CELL BIOLOGY

Caspase-3/7 deficiency results in enhanced intestinal inflammation and reduced tumorigenesis

Wei Xie[1,2], Laura Wyckaert[1,2], Mike Vadi[1,2], Bruno Verstraeten[1,2], Tatyana Divert[1,2], Jef Haerinck[2,3,4], Riet De Rycke[2,5], Femke Baeke[2,5], Mohamed Lamkanfi[6], Geert Berx[2,3,4], Adam Wahida[1,2,7], Peter Vandenabeele[1,2]*

Aberrant intestinal epithelial cell (IEC) death is common in inflammatory bowel disease (IBD) and related animal models. While various cell death pathways contribute to disease, the dominant modalities and their regulatory mechanisms in intestinal inflammation remain ill defined. Using the DSS colitis model, we examined the contribution of apoptosis (*Casp3/7*$^{\Delta IEC}$), necroptosis (*Mlkl*$^{\Delta IEC}$), pyroptosis (*Gsdme*$^{\Delta IEC}$, *Gsdmd*$^{-/-}$), and ferroptosis (*Gpx4*$^{i\Delta IEC}$) in IECs. Mice lacking caspase-3/7 in IECs showed worsened colitis, higher mortality, and impaired regeneration, not seen in the other transgenic mice. Caspase-3/7 deficiency in IECs hindered stem cell proliferation and increased inflammatory cell death, disrupting barrier integrity and delaying recovery. Despite heightened inflammation, *Casp3/7*$^{\Delta IEC}$ mice had reduced tumor formation in the AOM/DSS-induced colorectal cancer model. These findings highlight a protective role for caspase-3/7 in controlling inflammation and tissue regeneration, while promoting tumorigenesis following intestinal injury, and suggest modulation of caspase-3/7 as a promising therapeutic strategy in IBD and colorectal cancer.

INTRODUCTION

The intestinal epithelium consists of a single-cell monolayer of intestinal epithelial cells (IECs), which forms the cellular barrier between the luminal environment and the underlying lamina propria (*1*–*3*). Along with the mucus layer, it functions as a physical barrier against luminal contents, which, in some instances, may pose external threats such as microbes, dietary antigens, and toxins (*4*). At the same time, the intestinal mucosa facilitates communication between the gut microbiota and the host immune system to maintain intestinal homeostasis (*5*). Consequently, epithelial cells consist of various specialized cell populations, including enterocytes that take in nutrients as well as display antigens, mucus-secreting goblet, and epithelial Paneth cells that produce antimicrobial peptides (*2*). Despite these diverging functions, most IECs are rapidly renewed every 4 to 5 days through finely tuned regulatory processes involving stem cell proliferation, differentiation, and regulated cell death, which, in turn, are essential for preserving epithelial integrity during homeostasis (*1*).

Inflammatory bowel disease (IBD), comprising Crohn's disease (CD) and ulcerative colitis (UC), is a chronic and relapsing inflammatory disorder of the gastrointestinal tract (*5*–*7*). Alongside immune dysregulation and microbial imbalance, excessive and dysregulated epithelial cell death is a hallmark of IBD (*8*–*10*). Apoptosis and anoikis are traditionally understood as the predominant forms of IEC death under steady-state conditions. In contrast, several lines of evidence from experimental models and patient biopsies have implicated additional regulated cell death modalities, including necroptosis, pyroptosis, and ferroptosis, in disease pathology (*9*, *11*–*13*). Hence, the aberrant expression of key executioners and regulators, such as caspase-3 (*14*), caspase-7 (*15*), mixed-lineage kinase-like (MLKL) (*16*), gasdermins (*12*, *17*–*19*), and glutathione peroxidase 4 (GPX4) (*20*), suggests that multiple cell death programs may act in concert to drive intestinal inflammation. Still, their relative contribution to mucosal inflammation remains elusive.

Caspases 3 and 7, which represent the critical executioner caspases in apoptosis, are activated downstream of initiator caspases and cleave a broad range of substrates (*21*–*23*). Beyond their canonical role in cell death, they also influence cell proliferation, adhesion, and immune responses (*24*–*26*). On the contrary, the dysregulation of caspase-3/7 activity has been implicated in a diverse range of diseases, including cancer, autoimmune disorders, and infections (*27*–*29*). Thus, to investigate their specific role in the intestinal epithelium, we generated mice with IEC-specific deletion of *Casp3* and *Casp7* (*Casp3/7*$^{\Delta IEC}$). At steady state, these mice display no overt abnormalities in intestinal architecture or homeostasis, demonstrating that, in unchallenged mice, IEC apoptosis per se is dispensable for IEC turnover at the top of villi, intestinal tissue dynamics, the microbiome, and the gut immune cell composition (*30*). However, *Casp3/7*$^{\Delta IEC}$ mice are resistant to chemotherapy-induced gastrointestinal toxicity (*31*) and are highly susceptible to *Clostridium difficile* infection (*32*). Although prior work has suggested that systemic deletion of caspase-3 or caspase-7 enhances susceptibility to dextran sulfate sodium (DSS)–induced colitis (*15*, *33*), the cell type–specific contributions of caspase-3/7, particularly in IECs during IBD and colorectal cancer (CRC), remain unclear.

To interrogate the most consequential regulated cell death modalities side by side, we systematically compare the involvement of apoptosis, pyroptosis, necroptosis, and ferroptosis in a murine model of colitis and identify a uniquely heightened sensitivity in *Casp3/7*$^{\Delta IEC}$ mice. Scrutinizing caspase-3/7 deficiency in the gut under these circumstances revealed an impaired intestinal stem cell compartment, barrier integrity, and enhanced inflammation. In a CRC model, these mice exhibited reduced tumor burden, likely due to dysfunctional stem cell–driven regeneration.

---

[1] Molecular Signaling and Cell Death Unit, VIB-UGent Center for Inflammation Research, Flanders Institute for Biotechnology, Ghent, Belgium. [2] Department of Biomedical Molecular Biology, Ghent University, Ghent, Belgium. [3] Cancer Research Institute Ghent (CRIG), Ghent University, Ghent, Belgium. [4] Molecular and Cellular Oncology Laboratory, Ghent University, Ghent, Belgium. [5] VIB BioImaging Core, VIB-UGent Center for Inflammation Research, Technologiepark-Zwijnaarde 71, Ghent, 9052, Belgium. [6] Department of Internal Medicine and Pediatrics, Ghent University, Ghent, Belgium. [7] Institute of Metabolism and Cell Death, Molecular Targets and Therapeutics Center, Helmholtz Munich, Neuherberg, Germany.
*Corresponding author. Email: peter.vandenabeele@irc.vib-ugent.be

RESULTS

Excessive cell death in patients with IBD is associated with dysregulation of cell death executioners and key regulators

To explore the genome-wide association between cell death pathways and IBD, we analyzed the overlap between 319 IBD-associated genetic loci and the Gene Ontology (GO) term "cell death genes." This analysis identified 40 overlapping genes, including well-known regulators of cell death such as *BOK*, *BCL2L11* (also known as *BIM*), and *DAP1* (Fig. 1A). In addition, several genes involved in tumor necrosis factor (TNF) signaling and efferocytosis were identified, underscoring a putative role for cell death and inflammation regulation in IBD pathogenesis. We further assessed the overlap between cell death genes and differentially expressed (DE) genes in three independent transcriptomic datasets from patients with UC and CD. In all cohorts, more than 500 cell death–related genes were found among the DE genes (Fig. 1B), suggesting a widespread transcriptional modulation of cell death pathways in IBD. Notably, several key cell death executioner genes (*CASP3*, *CASP7*, *MLKL*, and *GSDME)* and the guardian of ferroptosis, *GPX4*, exhibited modulated expression patterns, albeit with some variability across datasets. To better understand the dynamics of these changes during intestinal inflammation, we analyzed the expression of six selected genes involved in the execution of cell death (*Casp3*, *Casp7*, *Mlkl*, *Gsdmd*, *Gsdme*, and *Gpx4*) in IECs from DSS-induced colitis mouse models using two publicly available single-cell RNA sequencing (RNA-seq) datasets (*34*, *35*). The expression patterns of these six genes appear to vary with disease progression, suggesting a possible association among these cell death pathways in the pathophysiology of colitis (Fig. 1C).

To further validate these findings experimentally, we induced DSS colitis in wild-type (WT) mice and analyzed protein expression of selected cell death markers in isolated colonic IECs (Fig. 1, D to H, and fig. S1A). DSS treatment led to activation of caspases 8, 3, and 7, indicative of apoptosis induction, whereas phosphorylated MLKL (pMLKL), a marker of necroptosis, was not detectable. Although GSDME proteolysis was not observed, high levels of p30 GSDMD were detected, suggesting a possible role for pyroptosis by generating the N-terminal pore-forming fragment of GSDMD. Regarding ferroptosis, although GPX4 protein levels remained unchanged over time, suggesting no central regulation at the protein expression level, its enzymatic activity could still be functionally relevant (*20*).

Casp3/7, but not *Mlkl*, *Gsdmd*, *Gsdme*, or *Gpx4*, determines DSS-induced colitis susceptibility

To dissect the possible roles of distinct IEC death modes in gut inflammation, we generated and analyzed the phenotype following DSS-induced colitis in a panel of transgenic mouse lines: $Casp3^{\Delta IEC}$, $Casp7^{\Delta IEC}$ and $Casp3/7^{\Delta IEC}$ (deficient in apoptosis executioners), $Mlkl^{\Delta IEC}$ and $Mlkl^{-/-}$ (deficient in necroptosis execution), $Gsdmd^{-/-}$ (deficient in pyroptosis execution), $Gsdme^{\Delta IEC}$ and $Gsdme^{-/-}$ (deficient in secondary necrosis/pyroptosis execution), and $Gpx4^{i\Delta IEC}$ and $Gpx4^{+/-\Delta IEC}$ (prone to ferroptosis). $Casp3/7^{\Delta IEC}$, $Mlkl^{\Delta IEC}$, $Gsdmd^{-/-}$, $Gsdme^{\Delta IEC}$, and $Gpx4^{i\Delta IEC}$ mice were subjected to a standardized experimental protocol consisting of 3% DSS treatment for 4 days, followed by a recovery phase with regular drinking water. In the context of deficiency of executioner caspases, $Casp3/7^{\Delta IEC}$ mice exhibited markedly worsened colitis compared to their cohoused $Casp3/7^{fl/fl}$ littermate controls. This was evidenced by rapid body weight loss, elevated disease activity index (DAI), and shortened colon length (Fig. 2A and fig. S2, A and B). Histological analysis revealed more extensive epithelial erosion, immune cell infiltration, and crypt loss in $Casp3/7^{\Delta IEC}$ mice, which was further corroborated by colonoscopy findings indicating ulceration, looser stool, and bleeding (Fig. 2B). Moreover, crypt deconstruction and barrier damage were more pronounced in $Casp3/7^{\Delta IEC}$ mice (fig. S1, B and C). Next, we also varied DSS concentrations and treatment durations to test whether the DSS regimen might affect the phenotype of $Casp3/7^{\Delta IEC}$ mice. Across these conditions, $Casp3/7^{\Delta IEC}$ mice consistently exhibited a robust inflammatory phenotype (fig. S1, D and E). Last, considering the phenotype of $Casp3/7^{\Delta IEC}$ mice, we investigated the relative contributions of caspase-3 and caspase-7 in the colitis model. To this end, $Casp3^{\Delta IEC}$, $Casp7^{\Delta IEC}$ mice and their cohoused littermates were subjected to DSS treatment. Different from $Casp3/7^{\Delta IEC}$ mice, neither *Casp3* nor *Casp7* deficiency alone in the IECs altered the host's sensitivity to DSS-induced colitis (fig. S1, F and G), suggesting functional redundancy between these apoptotic executioner caspases in IECs in returning to steady state following DSS-induced colitis.

To further explore the downstream consequences of apoptosis deficiency, we performed bulk RNA-seq of distal colon tissues from DSS-treated $Casp3/7^{\Delta IEC}$ mice and control littermates. RNA-seq identified substantial gene expression changes, including up-regulation of inflammatory and stress response genes and down-regulation of genes involved in epithelial function. Gene set enrichment analysis (GSEA) highlighted significant suppression of oxidative phosphorylation and fatty acid metabolism pathways. In contrast, epithelial-to-mesenchymal transition and inflammatory response pathways were notably up-regulated (Fig. 2C). These findings were validated by quantitative polymerase chain reaction (qPCR), which revealed reduced expression of the epithelial marker *Villin* and the resident intestinal stem cell marker *Lgr5*, alongside elevated expression of inflammatory cytokines *Il1b* and *Il6*, and altered expression of tight junction components *Zo1* and *Occludin* (Fig. 2D). To examine the possible role of necroptosis execution, we assessed $Mlkl^{\Delta IEC}$ mice. Mice lacking *Mlkl* in IECs showed no significant differences in weight loss, DAI, or colon length compared to their WT littermates. Histopathological evaluation confirmed similar mucosal damage across all DSS-treated groups, without genotype-specific differences (Fig. 2E and fig. S2C). Similarly, epithelial-specific deletion of *Gsdme* has limited influence on major disease parameters, indicating a negligible role for GSDME in this model (Fig. 2F and fig. S2, D and E). Although p30 GSDMD was generated following DSS treatment, indicative of proteolytic activation (Fig. 1H), $Gsdmd^{-/-}$ mice showed no significant difference in colitis severity compared to $Gsdmd^{+/+}$ controls under the same experimental conditions. Notably, both genotypes displayed relatively mild disease, suggesting that pyroptosis mediated by GSDMD may not considerably contribute to disease severity in this context of DSS-induced colitis (Fig. 2G and fig. S2, F to H).

The potential role of sensitized ferroptosis in IECs was examined by using $Gpx4^{i\Delta IEC}$ mice, in which *Gpx4* gene deletion in IECs was induced by tamoxifen injection (fig. S3A). Nonchallenged $Gpx4^{i\Delta IEC}$ mice exhibited no sign of either intestinal inflammation or systemic immune activation (fig. S3, B to G). In contrast to earlier studies (*20*), inducible *Gpx4* deficiency did not alter disease severity, as body weight, DAI, colon length, and histological scores were comparable to $Gpx4^{fl/fl}$ controls in DSS colitis (Fig. 2H and fig. S3, I and J). Of note, this mouse line exhibited heightened susceptibility to

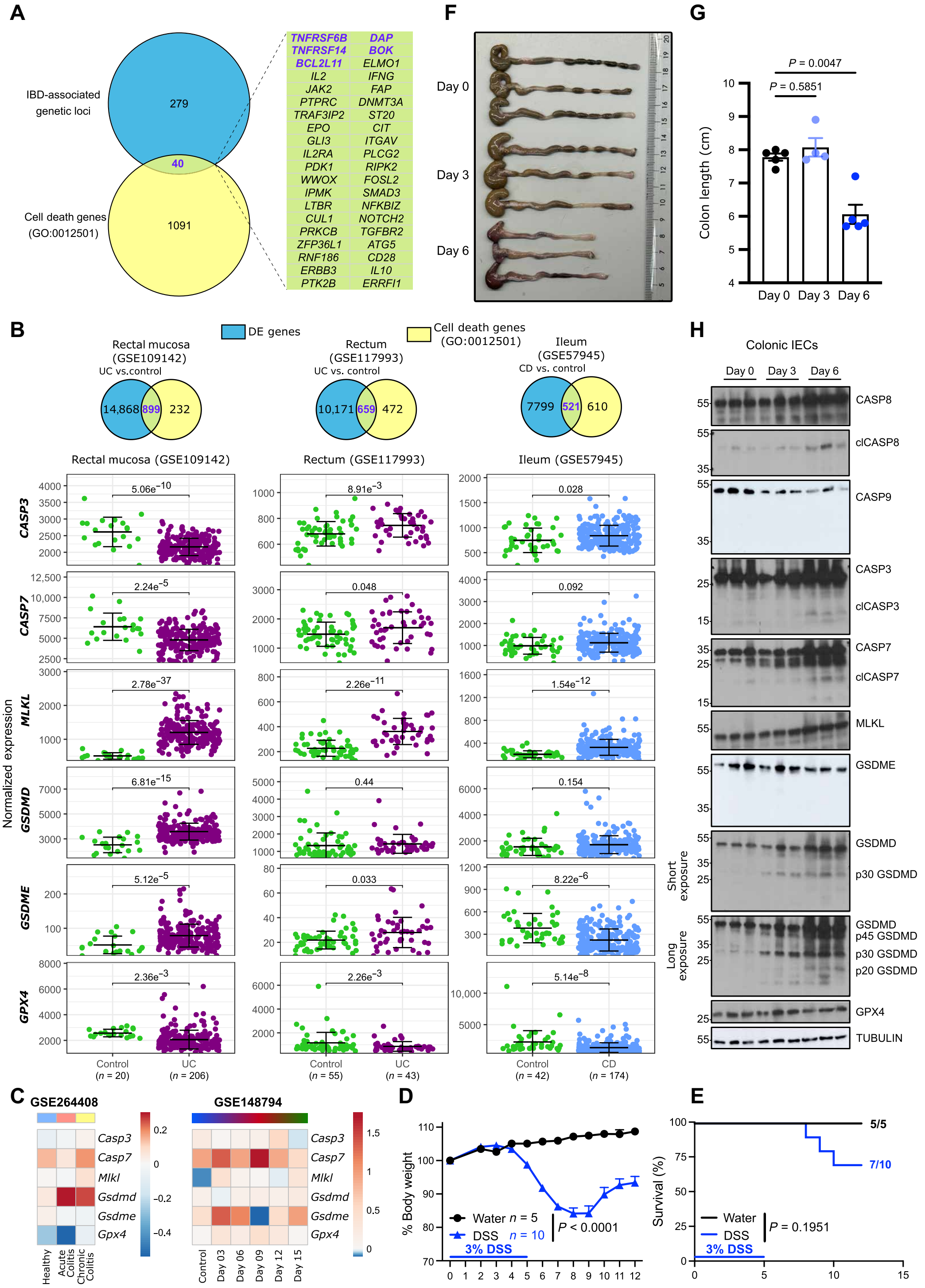

Fig. 1. Dysregulated cell death process in patients with IBD and experimental colitis mouse model. (**A**) Venn diagram shows the 40 genes overlapping the 319 IBD-associated genetic loci with the 1131 programmed cell death genes by GO (GO:0012501). (**B**) The top row shows the overlapping of DE genes ($P < 0.05$) from three different cohorts with programmed cell death genes (GO:0012501). Selected genes are shown for each cohort in a scatterplot using normalized gene expression values. (**C**) Average expression level of indicated genes in IECs from two single-cell RNA-seq datasets at different DSS colitis stages. (**D**) WT mice were treated with 3% DSS for 5 days, with monitoring of body weight changes and (**E**) survival. (**F**) Image of representative large intestine harvested on indicated days and (**G**) measurement of colon length ($n = 4$ to 5 per group). (**H**) Western blot using colonic IECs isolated from different days of mice in (D), cell death–related proteins were probed. TUBULIN was used as a loading control. Results are representative of data generated in two independent experiments. Error bars show means ± SD in (B). Error bars show mean ± SEM in (D) and (G). Statistical analysis of DE genes was performed using DESeq2 (B), body weight changes with a mixed-effects model (REML) analysis (D), Kaplan-Meier survival analysis (E), and one-way analysis of variance (ANOVA) for colon length (G). Data are representative of two independent experiments [(D) to (H)].

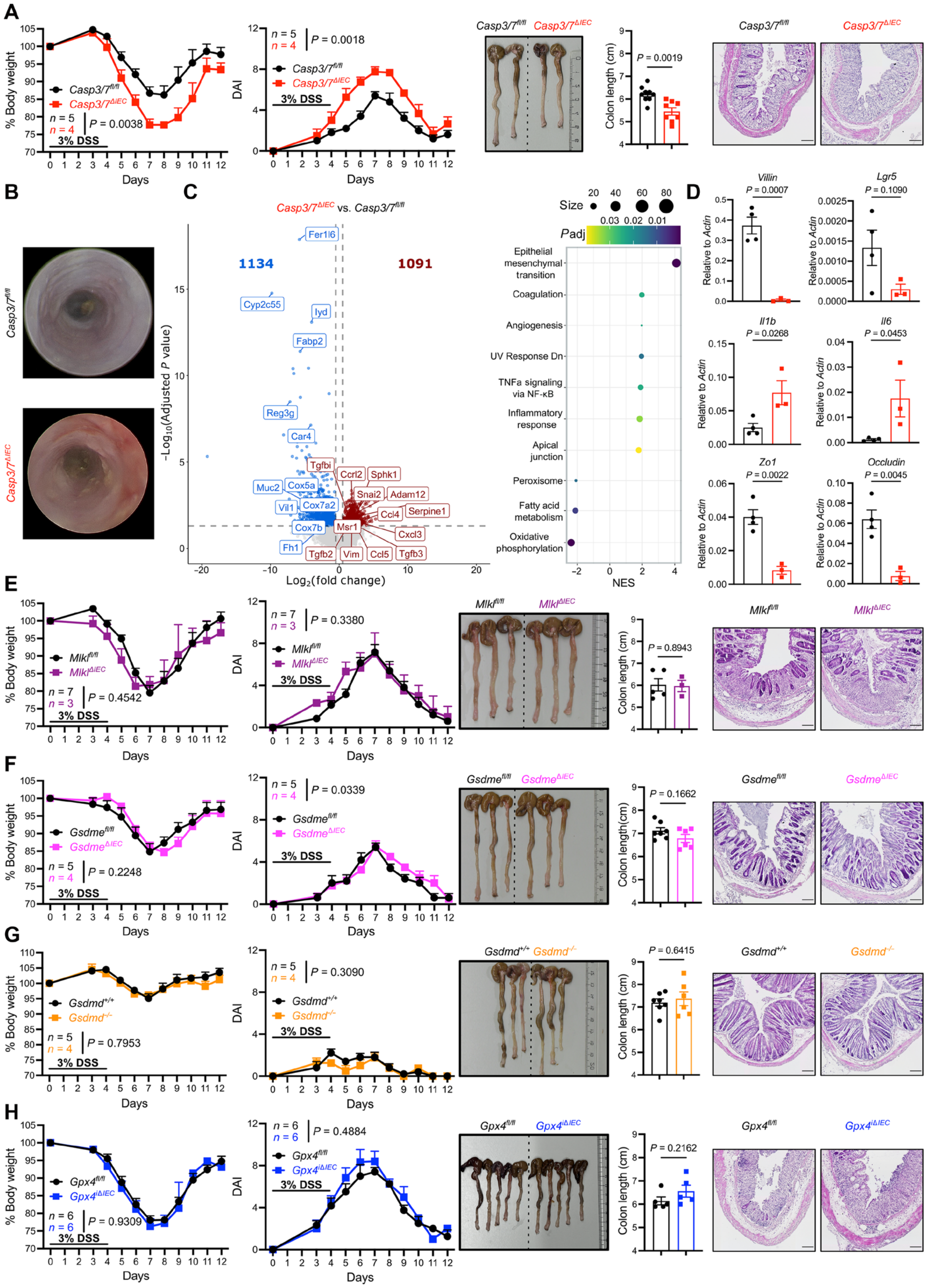

Fig. 2. Intestinal epithelium-specific depletion of Casp3/7, but not Mlkl, Gsdme, Gpx4, or full-body knockout of Gsdmd, sensitizes the host to DSS-induced colitis. (**A**) *Casp3/7*$^{\Delta IEC}$ and control mice were treated with 3% DSS in drinking water for 4 days, and body weight change and DAI were monitored over time. Colon picture, measurement of colon length, and representative H&E staining of distal colon tissue are shown. Data are representative of three independent experiments. (**B**) Representative endoscopic images of the colon of *Casp3/7*$^{fl/fl}$ and *Casp3/7*$^{\Delta IEC}$ mice on day 7. (**C**) Volcano plot analysis of the bulk RNA-seq dataset showing the top up-regulated and down-regulated genes in distal colon tissue of *Casp3/7*$^{\Delta IEC}$ mice compared to *Casp3/7*$^{fl/fl}$ mice (|log$_2$fold change| > 0.5, adjusted *P* value < 0.05, *n* = 5 to 6 per group). GSEA analysis revealing the enriched MSIGDB hallmark gene sets. UV, ultraviolet; Dn, down; NF-κB, nuclear factor κB; NES, normalized enrichment score. (**D**) mRNA expression relative to *Actb* in distal colon tissue of *Casp3/7*$^{fl/fl}$ and *Casp3/7*$^{\Delta IEC}$ mice on day 8 (*n* = 3 to 4 per group). Data are representative of two independent experiments. (**E**) *Mlkl*$^{\Delta IEC}$, (**F**) *Gsdme*$^{\Delta IEC}$, (**G**) *Gsdmd*$^{-/-}$, (**H**) *Gpx4*$^{i\Delta IEC}$ mice and their cohoused littermates were assessed in the same way as in (A). Results were generated with at least two cohorts. Data are representative of one [(F) to (H)] or two (E) independent experiments. *n* = 3 to 9 per group for colon length. Data are represented as mean ± SEM. Statistical analyses of body weight changes and DAI were performed using two-way ANOVA analysis in (F) and (G), with mixed-effects model (REML) analysis in (A), (E), and (H). Two-tailed unpaired Student's *t* tests were used for colon length and qPCR. Scale bars, 100 μm.

DSS-induced injury overall, regardless of *Gpx4* status in IECs, suggesting a genetic background-dependent effect in this model. Consistent with IEC-specific knockout lines, full-body knockout $Mlkl^{-/-}$, $Gsdme^{-/-}$ and heterozygous IEC knockout $Gpx4^{+/-\Delta IEC}$ mice did not display significant differences compared to controls in the DSS colitis model (fig. S1, H to J), also excluding a crucial contribution of necroptosis and pyroptosis by other cells than IECs in this model.

Together, these results paradoxically indicate that caspase-3/7 activity in IECs is critically involved in dampening the severity of DSS-induced colitis and facilitating faster recovery. At the same time, neither deficiency of necroptosis (MLKL), nor pyroptosis (GSDME and GSDMD), nor ferroptosis (GPX4) pathways seems to affect the phenotypic outcome of DSS colitis directly, suggesting a unique role for the apoptotic executioner caspases.

Ablation of *Casp3/7* leads to proliferation defects of ISCs and TACs

To systematically investigate the molecular basis of epithelial dysfunction in $Casp3/7^{\Delta IEC}$ mice, we performed bulk RNA-seq of IECs isolated from the distal colon at baseline (day 0) and during early colitis (day 3) (Fig. 3A). Consistent with previous findings (*30*), caspase-3/7 deletion in IECs had minimal impact on the epithelial transcriptome under steady-state conditions, as indicated by a limited number of DE genes (Fig. 3B). In contrast, DSS treatment revealed notable transcriptional differences between $Casp3/7^{\Delta IEC}$ mice and controls. Volcano plot analysis highlighted the suppression of key proliferation-related genes such as *Mki67*, *Stmn1*, *Pole*, *Cdk1*, and *Cdc20* (Fig. 3C). GSEA showed significant down-regulation of cell cycle–related pathways, including G_2M checkpoint, E2F targets, and mitotic spindle, in $Casp3/7^{\Delta IEC}$ IECs on day 3 (Fig. 3D). To assess whether other epithelial lineages were also affected, we looked at cell type–specific gene expression changes using the RNA-seq data (Fig. 3E). The transcriptional signature of intestinal stem cells (ISCs) and transient amplifying cells (TACs) was markedly diminished in $Casp3/7^{\Delta IEC}$ mice. In contrast, gene expression associated with terminally differentiated cell types, including goblet cells, enteroendocrine cells (EECs), tuft cells, and enterocytes, remained unchanged. We validated these observations by qPCR. Consistent with RNA-seq results, *Lgr5* (ISC marker) was significantly reduced at day 3 post-DSS. In contrast, expression of *Muc2* and *Tff3* (goblet cells), *Chga*, *Neurod1*, and *Sct* (EECs), and *Sis* (enterocytes) remained comparable across the genotypes studied (Fig. 3F).

Although no obvious histopathology was observed at this stage via hematoxylin and eosin (H&E) staining (Fig. 3G), staining of Ki67 revealed a significant reduction in proliferating ISCs and TACs in $Casp3/7^{\Delta IEC}$ mice (Fig. 3, H and I). To further explore whether the reduction in ISCs and TACs results in more severe disease, $Casp3/7^{\Delta IEC}$ mice and controls were treated with 3% DSS for 3 days, followed by a switch to regular drinking water. Under these conditions, $Casp3/7^{\Delta IEC}$ mice lost more body weight and had a higher disease score (fig. S4, A and B). Notably, increased intestinal permeability was observed in $Casp3/7^{\Delta IEC}$ mice compared to controls post-DSS treatment (fig. S4C), indicating defects in barrier function. To investigate the potential mechanism behind this proliferation defect, we generated colonic organoids ex vivo. Consistent with our previous finding, the absence of caspase-3/7 has no impact on colonic organoid formation capacity and growth speed at steady state (fig. S4, D and E) (*30*). Next, we attempted to evaluate how the addition of DSS may affect organoid growth in vitro, as reported previously (*36*, *37*). However, the Matrigel began to disintegrate shortly after low-concentration DSS treatment (0.001%), causing difficulties in recapitulating an in vitro DSS model (fig. S4F). So, the in vivo results indicate that caspase-3/7 deficiency in IECs selectively impairs ISC and TAC proliferation during early DSS-induced colitis, without affecting the differentiation or maintenance of mature epithelial lineages (Fig. 3, E and F).

Casp3/7 deletion in IECs has no impact on overall cell death events

As apoptosis represents a crucial mode of IEC death during DSS-induced colitis (*38*), we next sought to quantify IEC cell death in $Casp3/7^{fl/fl}$ and $Casp3/7^{\Delta IEC}$ mice. Terminal deoxynucleotidyl transferase–mediated deoxyuridine triphosphate nick end labeling (TUNEL) staining revealed comparable levels of IEC death across genotypes, both with and without DSS administration (fig. S5, A and B). This unexpected result suggests that, in the absence of *Casp3/7*, alternative cell death modalities may compensate for the loss of apoptosis. To further assess IEC death ex vivo, we derived colonic organoids from $Casp3/7^{\Delta IEC}$ and control mice and treated them with mouse TNF and interferon-γ to induce cell death pathways. Organoid viability was unaffected by *Casp3/7* deficiency under these conditions, indicating no significant difference in overall cell death rates (fig. S5, C and D), consistent with our previous report at steady state in vivo (*30*). Given that apoptosis is typically immunologically silent, we hypothesized that proinflammatory forms of cell death, specifically pyroptosis and necroptosis, may account for the increased inflammation observed in $Casp3/7^{\Delta IEC}$ mice, consistent with bulk RNA-seq signatures (Fig. 3, C and D). To test this, we examined canonical markers of apoptosis, necroptosis, and pyroptosis in IECs via immunoblotting.

In line with our prior observations (Fig. 1H), DSS treatment induced caspase-8–mediated apoptosis in IECs, as evidenced by activation of caspase-8, caspase-3, and caspase-7 (fig. S5E). Notably, we detected no phosphorylated RIPK1 or MLKL, and caspase-8 activation remained intact in $Casp3/7^{\Delta IEC}$ mice, suggesting that necroptosis is not engaged in the absence of caspase-3/7. To confirm this, we generated $Casp3/7/Mlkl^{\Delta IEC}$ mice lacking both apoptotic and necroptotic pathways. These mice exhibited identical sensitivity to DSS-induced colitis as $Casp3/7^{\Delta IEC}$ mice, reinforcing that necroptosis does not compensate for apoptosis loss in this setting (fig. S5, F and G).

We also explored whether GSDMD might contribute to the phenotype of $Casp3/7^{\Delta IEC}$ mice as a potential compensatory mechanism for the lack of apoptosis execution. Pyroptosis is executed by a p30 fragment of GSDMD, which is produced by inflammatory caspases at Asp^{276} (*39*, *40*). Caspase-3/7 has previously been shown to inhibit murine GSDMD activity by cleaving it at Asp^{88}, generating an inactive p20 fragment of GSDMD that cannot form pores (*41*–*43*). Following DSS treatment in $Casp3/7^{fl/fl}$ and $Casp3/7^{\Delta IEC}$ mice, we detected caspase-1/11/8 activation and the generation of the pyroptotic effector GSDMD p30 fragment, while GSDME was not cleaved (fig. S5E). In $Casp3/7^{\Delta IEC}$ mice, we observed a comparable abundance of the active GSDMD p30 fragment in the IECs following DSS administration. Still, the inactive GSDMD p20 fragment was apparently absent, indicating that possibly an increase in the p30/p20 GSDMD ratio may contribute to inflammatory cell death during DSS colitis in $Casp3/7^{\Delta IEC}$ mice.

To validate a possible functional contribution of GSDMD in vivo, we administered disulfiram to $Casp3/7^{\Delta IEC}$ mice during DSS-

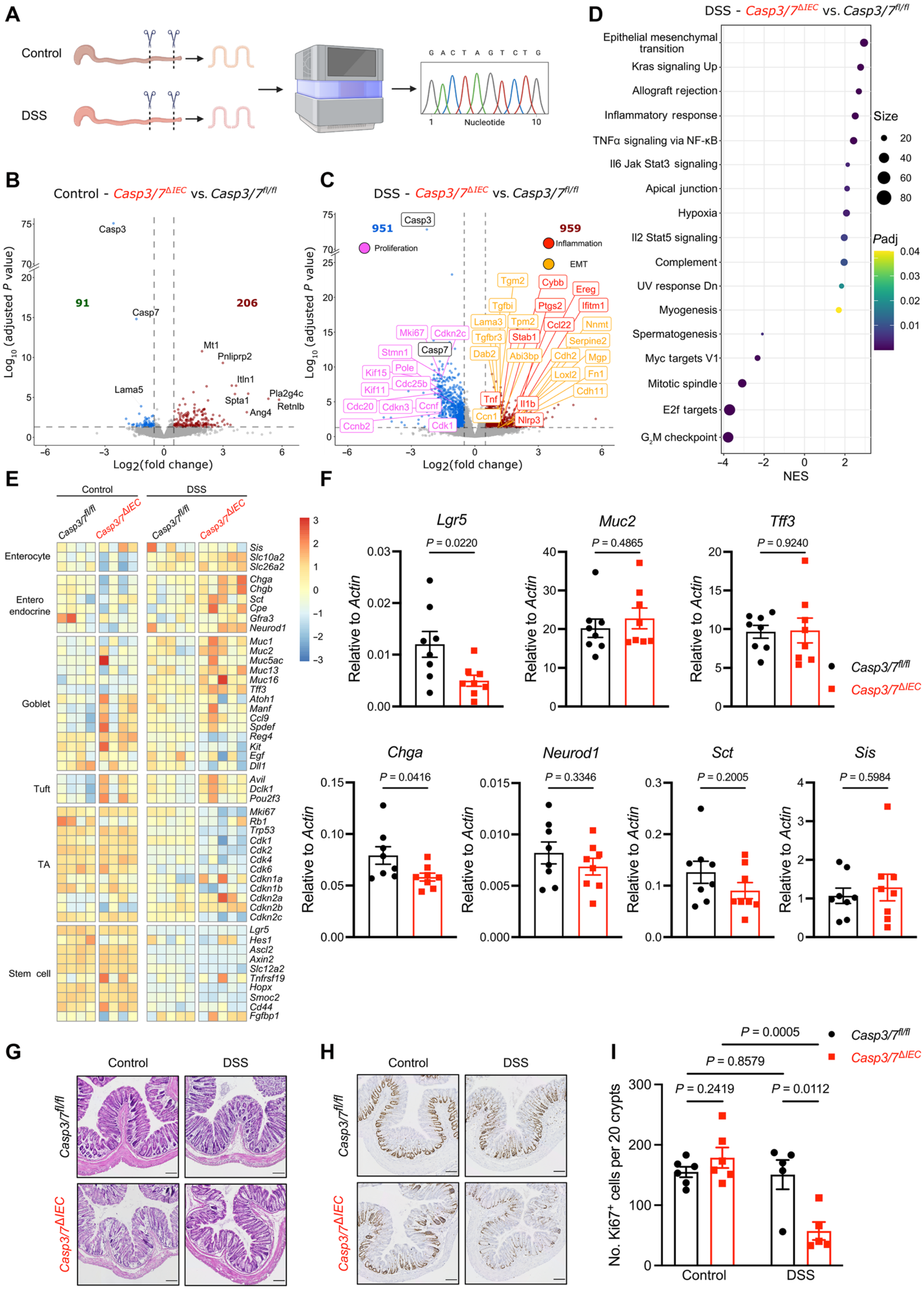

Fig. 3. Increased sensitivity to colitis in *Casp3/7*$^{\Delta IEC}$ mice is associated with aberrant ISC and TAC homeostasis. (**A**) Experimental design illustrating the isolation of colonic IECs from naïve or DSS treated mice at day 3 for bulk RNA-seq. Created in BioRender (https://BioRender.com/r8crwyg). (**B**) Volcano plot analysis of the bulk RNA-seq dataset showing the top up-regulated and down-regulated genes at steady state ($n = 4$ per group) and (**C**) typical genes from three different pathways post-DSS treatment ($n = 5$ per group) in IECs of *Casp3/7*$^{\Delta IEC}$ mice compared to *Casp3/7*$^{fl/fl}$ mice ($|\log_2 \text{fold change}| > 0.5$, adjusted P value < 0.05). (**D**) GSEA analysis revealing enriched MSIGDB hallmark gene sets post-DSS treatment. (**E**) Heatmap analysis of the RNA-seq dataset displaying marker genes for IEC lines in *Casp3/7*$^{fl/fl}$ and *Casp3/7*$^{\Delta IEC}$ mice. TA, transient amplifying. (**F**) mRNA expression of typical cell type marker genes in IECs isolated from DSS-treated mice ($n = 8$ per group). Data represent two pooled experiments. (**G**) Representative H&E staining and (**H**) proliferation marker Ki67 staining of distal colon tissue. (**I**) Quantification of Ki67 positivity ($n = 5$ to 6 per group). Data represent two pooled experiments [(H) and (I)]. Data are represented as mean ± SEM. Statistical analyses of qPCR and Ki67 counting were performed using a two-tailed unpaired Student's *t* test. Scale bars, 100 μm.

induced colitis (fig. S6A). Disulfiram is a clinically approved thiol-reactive drug that covalently modifies Cys^{192} (corresponding to Cys^{191} in human GSDMD) to inhibit GSDMD pore activity (*44*), besides many other thiol group–containing protein targets (*45*, *46*). Disulfiram treatment significantly abrogated the difference in colitis severity in *Casp3/7*$^{\Delta IEC}$ mice compared to vehicle controls (fig. S6B). Disulfiram also restored colon length (fig. S6, C and D) and improved histological architecture, with better epithelial integrity and reduced immune infiltration (fig. S6E). Furthermore, qPCR analysis revealed reduced mRNA levels of proinflammatory cytokine *Il6* and chemokine *Cxcl1* in colonic tissues from the disulfiram-treated group (fig. S6F). Together, these findings show that caspase-3/7 does not restrict colonic inflammation by preventing the level of IEC cell death per se, but rather by hindering enhanced inflammatory cell death by non-IEC cells that could be prevented by disulfiram treatment.

Epithelial caspase-3/7 promotes inflammation-associated intestinal carcinogenesis

Chronic intestinal inflammation is a well-established risk factor for carcinogenesis, with patients suffering from IBD exhibiting a heightened incidence of CRC (*47*, *48*). Tumor development typically requires two key processes: the accumulation of genetic mutations and a protumorigenic inflammatory or injured environment that promotes the expansion of mutated cells. The azoxymethane (AOM)/DSS model recapitulates this sequence, where AOM-induced mutations are followed by cycles of DSS-driven inflammation to stimulate tumor growth, mirroring the pathogenesis of colitis-associated CRC in humans. Given our previous observation that *Casp3/7*$^{\Delta IEC}$ mice display heightened intestinal inflammation but impaired proliferation of stem and TACs during acute DSS colitis (Fig. 3, C to F), we sought to determine which of these opposing effects predominates in the context of chronic tumorigenesis. Thus, we subjected *Casp3/7*$^{\Delta IEC}$ and *Casp3/7*$^{fl/fl}$ control mice to the AOM/DSS protocol (Fig. 4A). Unexpectedly, *Casp3/7*$^{\Delta IEC}$ mice developed significantly fewer tumors than controls, with a marked reduction in the larger tumor category (Fig. 4, B and C). The total tumor burden, as assessed by cumulative tumor volume, was also markedly lower in these mice (Fig. 4D). Histopathological analysis revealed that aggressive carcinomas were frequently observed in control animals, whereas *Casp3/7*$^{\Delta IEC}$ mice exhibited milder lesions (Fig. 4E). Immunohistochemical staining further demonstrated reduced proliferative activity within tumor regions of *Casp3/7*$^{\Delta IEC}$ mice (Fig. 4F), supporting the conclusion that defective epithelial regeneration due to impaired stem cell and TAC function, rather than enhanced inflammation alone, determines tumor outgrowth in this model. Moreover, the reduced tumors in *Casp3/7*$^{\Delta IEC}$ mice are caspase-3/7 deficient, indicating that they originate from IECs (Fig. 4G).

Our results suggest that caspase-3/7 deficiency impairs epithelial proliferation and stemness. Despite exacerbated inflammation and barrier dysfunction, this impairment appears to reduce inflammation-driven colorectal tumorigenesis by limiting resident stemness and the expansion of premalignant clones (Fig. 4H).

A dispensable role of epithelial GPX4 in x-ray–induced injury and development of AOM/DSS CRC

Dysregulated GPX4 abundance and activity have been associated with several intestinal diseases, indicating ferroptosis as a potential therapeutic target, but the genetic evidence for the implication is lacking (*20*, *49*–*51*). Here, our data indicate that GPX4 deficiency in IECs does not affect the intestinal steady state (fig. S3). No difference in susceptibility was observed in the DSS colitis model, ruling out a role for GPX4 (Fig. 2H). Apart from acute colitis, we further used a whole-abdomen irradiation model, as ferroptosis induction has been implicated in radiation-induced cell death (*52*–*56*). Epithelial GPX4 deficiency has no significant pathophysiological impact on intact gastrointestinal x-ray sensitivity, as shown by body weight measurements (Fig. 5, A and B). Given the potential tumor-suppressive role of ferroptosis induction in CRC (*57*, *58*), we examined whether *Gpx4* deficiency in IECs would negatively affect AOM/DSS-induced CRC development. However, no difference was seen between control and tamoxifen-induced GPX4 deficiency in *Gpx4*$^{i\Delta IEC}$ mice, suggesting no crucial role of GPX4 in AOM/DSS tumorigenesis (Fig. 5, C to G). Together, our study argues the noncrucial role of GPX4 in the gut epithelium during radiation-induced injury and inflammation-associated CRC development.

DISCUSSION

IEC turnover is a tightly regulated process that ensures gut integrity and function. While apoptosis has long been recognized as the primary form of IEC death under physiological and pathological conditions, recent studies have suggested that alternative regulated cell death pathways, including necroptosis, pyroptosis, and ferroptosis, may play context-dependent roles during intestinal inflammation or injury (*11*–*13*). However, the relative contribution of each cell death mode, particularly in IECs during IBD, remains incompletely understood. Using a panel of genetically engineered mouse models, we identify the combination of caspases 3 and 7 as a critical determinant of IEC homeostasis, epithelial regeneration, and immune tolerance during intestinal inflammation and tumorigenesis.

Our comparison of cell death–deficient mouse lines under a standardized DSS colitis model revealed an exacerbated inflammatory phenotype in *Casp3/7*$^{\Delta IEC}$ mice, while mice deficient in necroptosis (*Mlkl*$^{\Delta IEC}$), pyroptosis (*Gsdmd*$^{-/-}$), secondary necrosis/pyroptosis (*Gsdme*$^{\Delta IEC}$), or ferroptosis regulators (*Gpx4*$^{i\Delta IEC}$) exhibited no significant differences compared to the littermate controls. This suggests that, under these conditions, apoptosis plays a nonredundant and protective role, whereas other death pathways are either dispensable or effectively suppressed by compensatory mechanisms. Transcriptomic and histological analyses provided mechanistic insights into this phenotype. We show that *Casp3/7* genes are essential for maintaining the proliferation of ISCs and TACs during injury-induced regeneration. Despite no observable phenotype at steady state (*30*), *Casp3/7*$^{\Delta IEC}$ mice exhibit transcriptional repression of cell cycle pathways and reduced expression of proliferation markers post-DSS, particularly within ISC and TAC compartments, without affecting terminally differentiated IEC lineages. This suggests a selective requirement for caspase-3/7 in regenerative epithelial proliferation, possibly through nonapoptotic roles of caspases in cell cycle regulation. This could include the phenomenon of apoptosis-induced compensatory proliferation (AiP) (*59*, *60*).

Although caspase-3/7–mediated apoptosis was recognized as a primary cell death modality in this model, a comparable number of dying IECs were observed in *Casp3/7*$^{\Delta IEC}$ and control mice, as evidenced by TUNEL staining and organoid viability. To further assess whether the qualitative nature of cell death was altered in *Casp3/7*$^{\Delta IEC}$ mice, we analyzed other cell death markers. The generation of p20 GSDMD due to caspase-3/7 cleavage at Asp^{88} was entirely absent in

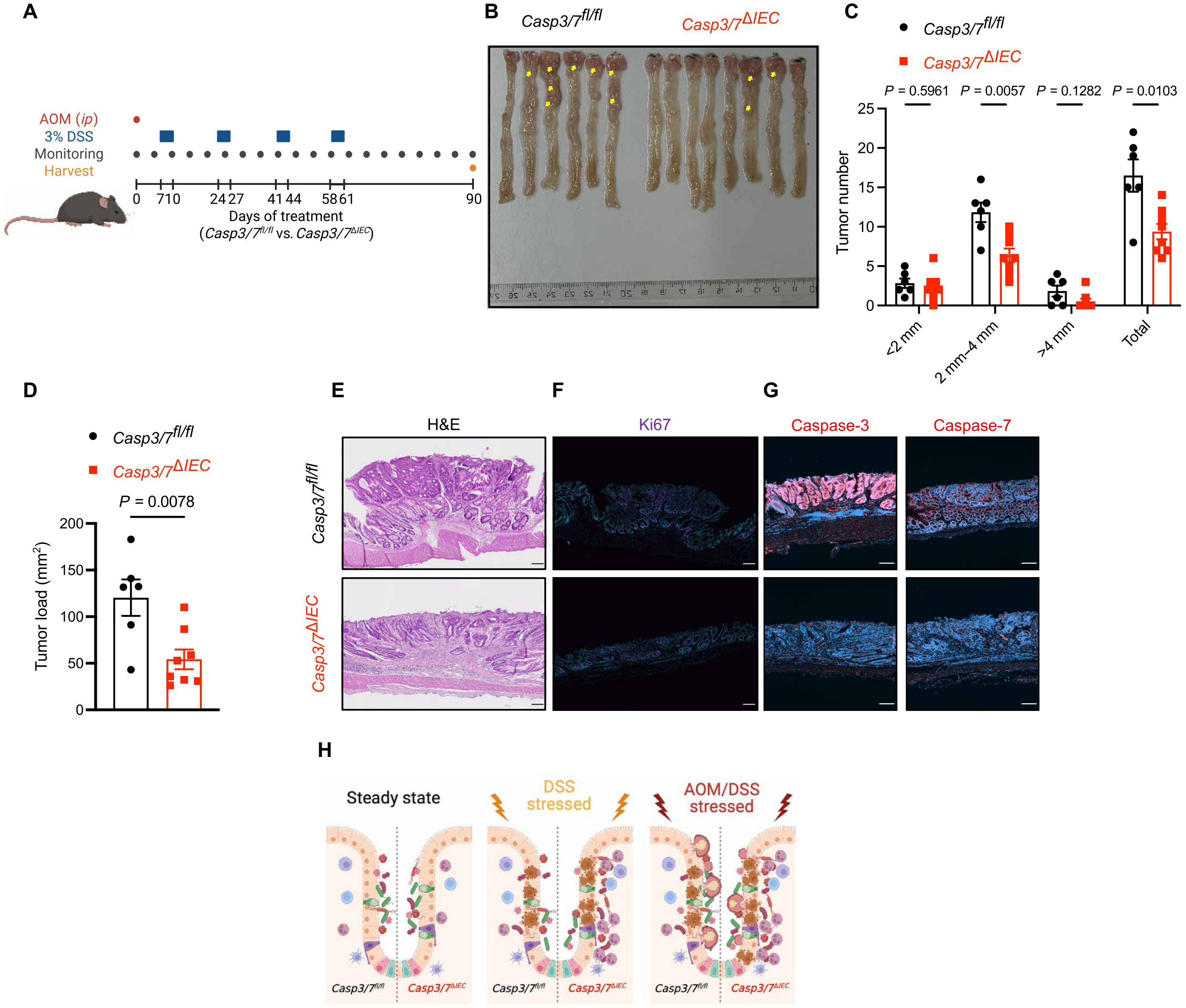

Fig. 4. Caspase-3/7 depletion reduces AOM/DSS-induced colitis-associated CRC. (**A**) Mice received a single injection of AOM, followed by four rounds of DSS to induce colitis-associated CRC. Created in BioRender (https://BioRender.com/cyvvh24). ip, intraperitoneal. (**B**) Image of colon with tumors from *Casp3/7*$^{\Delta IEC}$ and *Casp3/7*$^{fl/fl}$ mice on day 90. Arrows indicate large tumors. (**C**) Number of tumors in different sizes and total amount (*n* = 6 to 8 per group). (**D**) Overall tumor load (in square millimeters). (**E**) Representative histopathology images of colon tumors. (**F** and **G**) Immunofluorescent staining of Ki67-positive proliferating cells, caspase-3 and caspase-7. (**H**) Mice with caspase-3/7 deficiency in IECs have no abnormal phenotype at steady state. In the context of the DSS challenge, ISCs and TACs lacking caspase-3/7 were unable to proliferate actively, leading to barrier dysfunction. Meanwhile, the absence of caspase-3/7 leads to an aberrant increase in GSDMD-mediated pyroptosis, which aggravates intestinal inflammation. Because of impaired ISC function, *Casp3/7*$^{\Delta IEC}$ mice developed fewer tumors in a CAC model. Created in BioRender (https://BioRender.com/b2uvo83). Data are represented as mean ± SEM. Two-tailed unpaired Student's *t* tests were used for tumor number and load quantification. Scale bars, 100 μm. Data represent one experiment.

Casp3/7$^{\Delta IEC}$ IECs. In contrast, the generation of p30 GSDMD remained at a similar level, suggesting a comparable level of pyroptosis potential in both *Casp3/7*$^{\Delta IEC}$ and *Casp3/7*$^{fl/fl}$ littermates. However, the phenotypic difference in DSS-induced colitis between the two strains suggests that additional caspase-3/7–mediated mechanisms might be implicated in chronic intestinal inflammation in the context of IEC. Reduced regenerative potential may further affect inflammation by impairing barrier renewal. Paradoxically, while *Casp3/7*$^{\Delta IEC}$ mice suffered from more severe colitis, they exhibited reduced colitis-associated tumorigenesis in the AOM/DSS model. This result again underscores the dual role of caspase-3/7 in IECs: on the one hand, limiting inflammation; on the other, paradoxically supporting tumorigenesis by maintaining stem cell–driven regeneration. Despite heightened inflammation, the reduced tumor burden and proliferation in *Casp3/7*$^{\Delta IEC}$ mice argue that impaired epithelial repair and clonal expansion, rather than enhanced inflammation, drive

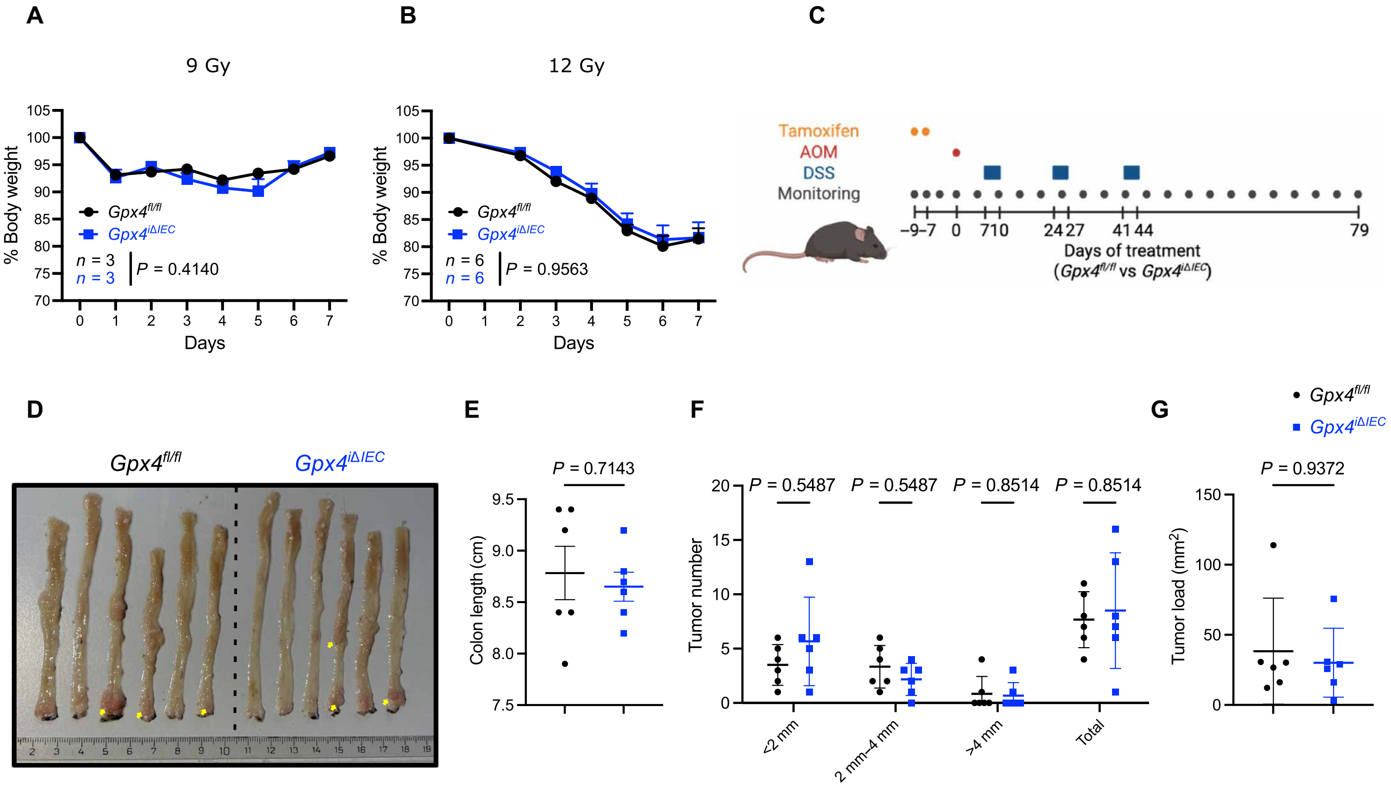

Fig. 5. Epithelial GPX4 is dispensable in x-ray–induced injury and development of AOM/DSS CRC. (**A**) Mice received 9 Gy ($n = 3$ per group) or (**B**) 12 Gy ($n = 6$ per group) whole abdomen irradiation, followed by 7 days of recovery. (**C**) Tamoxifen-treated mice received a single injection of AOM, followed by three rounds of DSS to induce colitis-associated CRC. Created in BioRender (https://BioRender.com/pwg2odd). (**D**) Image of colon with tumors from *Gpx4*$^{i\Delta IEC}$ and *Gpx4*$^{fl/fl}$ mice on day 79. Arrows indicate large tumors. (**E**) Measurement of colon length ($n = 6$ per group). (**F**) Number of tumors in different sizes and total amount ($n = 6$ per group). (**G**) Overall tumor load (in square millimeters) ($n = 6$ per group). Data are represented as mean ± SEM. Statistical analyses of body weight changes were performed using a two-way ANOVA (A) and a mixed-effects model (REML) (B). Two-tailed unpaired Student's *t* tests were used for tumor number and load quantification. Data represent one experiment.

neoplastic progression in this setting. The absence of caspase-3 and caspase-7 expression in tumors confirmed their outgrowth from *Casp3/7*$^{\Delta IEC}$ progenitors.

Although the mechanisms by which caspase-3/7 regulates cell death and proliferation have been extensively investigated in vitro, studies using caspase-3/7–deficient hosts remain limited in cancer research (*61*). *Casp3*$^{-/-}$ and *Casp7*$^{-/-}$ mice are resistant to DMBA/TPA-induced skin carcinogenesis, due to reduced endonuclease G–mediated genetic instability (*62*). As genomic instability is a feature of the AOM/DSS mouse model, in which the somatic mutation burden is comparable to that of human microsatellite instability-high (MSI-H) CRC (*63*), this mechanism thus may also contribute to the phenotype of our *Casp3/7*$^{\Delta IEC}$ mice, together with a lower level of AiP (*59*, *60*).

GPX4 is the guardian of ferroptosis and critical for embryonic development (*64*–*68*). Although the surviving *GPX4*$^{\Delta IEC}$ puppies were born smaller, they reached similar body weight at 7 weeks and exhibited normal gastrointestinal tract morphology compared to their WT littermate controls, arguing for a redundant role of epithelial GPX4 in adult mice at steady state. In line with this finding, our study shows that inducible GPX4 knockout in gut epithelium has no major impact. Ionizing radiation induces massive reactive oxygen species and lipid peroxidation, whereas GPX4 converts lipid hydroperoxides into lipid alcohols, thereby preventing ferroptosis and mitigating tissue damage (*52*, *67*, *69*, *70*). Pharmacological modulation of GPX4 activity or abundance has been shown to affect ionizing radiation-induced intestinal injury, although the genetic evidence remains insufficient (*71*, *72*). Mice lacking GPX4 in the epithelium did not exhibit more severe disease activity or delayed recovery. As a recently described cell death modality with distinct mechanisms, ferroptosis-induced cancer therapy has been a heavily researched topic for years, potentially by targeting GPX4 (*73*–*75*). GPX4 expression is up-regulated in CRC tissue, and its high expression is correlated with poor prognosis (*76*, *77*), implying that GPX4 may be involved in CRC development. However, our AOM/DSS results suggest that the absence of GPX4 has no noticeable impact on CRC development, as evidenced by comparable tumor numbers and burden between *Gpx4*$^{i\Delta IEC}$ and controls. These observations suggest that targeting GPX4 for gastrointestinal tract-related diseases should be critically reconsidered.

From a translational perspective, our findings put forward a framework that invites contemplation of modulating caspase-3 and caspase-7 activity to provide a therapeutic benefit in IBD or inflammation-associated CRC, depending on the disease context. For example, one could stipulate from our data that enhancing caspase-3 and -7 activity might suppress inflammatory pyroptosis in active colitis, while a more transient inhibition could harness protective cues against chemotherapy-induced toxicity (*32*) or even limit epithelial hyperproliferation in cancer. However, the nonredundant and highly context-dependent roles of caspase-3 and -7 also strongly caution against indiscriminate targeting and rather argue in favor of cell type– and disease stage–specific strategies. In conclusion, our study identifies that caspase-3 and -7 are central regulators of intestinal epithelial fate, matching inflammatory signaling and regenerative capacity through a dual control of stem cell proliferation and inflammatory (pyroptotic) restraint. These insights offer a more nuanced understanding of cell death dynamics in the intestinal epithelium and open previously unexplored avenues for targeted interventions in IBD and CRC.

Limitations of this study

This work has several limitations. First, our results are generated primarily on DSS-induced colitis and AOM/DSS-driven colorectal tumorigenesis models, which, while being widely used and validated, do not fully reflect the complexity of human IBD or CRC. Particularly in IBD, genetic variants leading to a propensity to undergo necroptosis have been reported, which nuances the scope of DSS-based experiments in the context of this disease spectrum. Second, our study uses a conditional knockout approach that limits *Casp3/7* deletion to IEC expressing Villin, thereby ruling out a possible role for stromal or immune cell–derived factors. In addition, it must be noted that different recombination efficiencies, as a function of time or the method of temporally controlled deletion, as seen in our inducible models such as *Gpx4*$^{i\Delta IEC}$, may impart a degree of "variability" to the specificity of our gene ablation experiments. Third, while it appears that there is a definite impairment in proliferation as well as a distinct inflammatory "signature" as determined by a variety of RNA expression analyses, it remains unresolved under which pathway or mechanism, such as nonapoptotic signaling, altered yes-associated protein expression, or AiP (*24*–*26*), caspase-3/7 appears to modulate the regulation of ISC homeostasis.

MATERIALS AND METHODS

Analysis of public datasets

The overlap of IBD-associated genetic loci and cell death loci was analyzed by taking the loci annotated as IBD-associated by Liu *et al.* (*78*) and searching for overlap with the set of genes annotated as programmed cell death genes by GO as taken from AmiGO 2 using the filters organism: *Homo sapiens* and type: protein. Overlap was determined by comparing sets of gene symbols. Further association between cell death genes and IBD was investigated using RNA-seq data of patients with UC or CD and their respective controls (*79*–*81*). Differential expression analysis was performed by downloading the Gene Expression Omnibus (GEO) raw counts and using DESeq2 (v1.46.0) (*82*). The *P* values on the scatterplots are adjusted *P* values as calculated by DESeq2. Error bars indicate SD. Last, single-cell sequencing data of murine DSS-induced UC samples (*34*, *35*) were processed using Seurat (v5.2.0) (*83*). Quality control was performed by calculating mitochondrial gene expression using the PercentageFeatureSet function and filtering the cells using the following thresholds: nFeature_RNA > 200, nFeature_RNA < 2500, percent.mt < 5. Afterward, data were normalized and scaled using the following: NormalizeData (SeuratOjb), FindVariableFeatures (SeuratObj, selection.method = "vst," nFeatures = 2000), ScaleData [SeuratObj, features = rownames(SeuratObj)]. Heatmaps represent averaged scaled expression values.

Mice

Casp3/7$^{fl/fl}$ (*30*), *Casp3/7/Mlkl*$^{fl/fl}$ (*30*), *Gpx4*$^{fl/fl}$ (*66*), and *Gsdmd*$^{-/-}$ (*39*, *40*) mice were described previously. *Mlkl/*$^{-/-}$ and *Mlkl*$^{fl/fl}$ mice were obtained from J. M. Murphy (Walter and Eliza Hall Institute of Medical Research) (*84*). *Dfna5tm1a*(KOMP)Wtsi ES cells were obtained from the European Conditional Mouse Mutagenesis Program and established in a C57Bl6 background. *Gsdme*$^{tm1a(KOMP)Wtsi}$ mice were crossed with C57BL/6-Tg(CAG-Flpo)1Afst/Ieg tg/ + mice to obtain the *Gsdme*$^{tm1c(KOMP)Wtsi}$ floxed allele. The *Gsdme*$^{tm1d(KOMP)Wtsi}$ knockout allele was obtained by crossing *Gsdme*$^{tm1c(KOMP)Wtsi}$ mice with C57BL/6J-*Edil3*$^{Tg(Sox2\text{-}cre)1Amc}$/J. *Casp3*$^{fl/fl}$ and *Casp7*$^{fl/fl}$ mice were generated by crossing *Casp3/7*$^{fl/fl}$ mice with WT mice. *Casp3/7*$^{\Delta IEC}$, *Casp3*$^{\Delta IEC}$, *Casp7*$^{\Delta IEC}$, *Casp3/7/Mlkl*$^{\Delta IEC}$, *Mlkl*$^{\Delta IEC}$, *Gsdme*$^{\Delta IEC}$, and *Gpx4*$^{+/-\Delta IEC}$ mice were obtained by crossing to *Vil1-Cre* mice. *Gpx4*$^{i\Delta IEC}$ mice were obtained by crossing to *Vil1-CreERT2* mice. To deplete *Gpx4*, *Gpx4*$^{i\Delta IEC}$ mice and control were intraperitoneally injected with 2 mg of tamoxifen dissolved in corn oil on day 0 and day 2, *Gpx4* was knocked out, and mice were subjected to treatment from day 9. Mice were bred in-house using heterozygous breeding pairs to obtain transgenic and WT littermate controls in the Flemish Institute for Biotechnology (VIB) Center for Inflammation Research under specific pathogen–free conditions. C57BL6/N WT mice were purchased from JANVIER LABS and acclimated for at least 1 week before the start of any experiment. All experiments on mice were conducted according to institutional, national, and European animal regulations. The local Ethics Committee of Ghent University approved animal protocols (study approval numbers: LP0024, 2025-003, 2025-037, and 2025-097). Sex-matched and age-matched cohoused littermates were used throughout the entire study, except as further indicated.

DSS-induced colitis model

Both male and female cohoused littermates received 2 or 3% DSS salt (160110, MP Biomedicals) for 3, 4, or 5 days as indicated in the experimental scheme, followed by normal drinking water until the end of the experiment. To assess the severity of colitis, body weight loss (<5%, score 0; 5 to 10%, score 1; 10 to 15%, score 2; 15 to 20%, score 3; >20%, score 4), stool consistency (normal, score 0; soft but still formed, score 1; very soft, score 2; diarrhea, score 3; dysenteric diarrhea, score 4), and bleeding (negative hemoccult, score 0; positive hemoccult, score 1; blood traces in stool visible, score 2; mild rectal bleeding, score 3; rectal bleeding, score 4) were monitored daily. DAI is the sum of the three parameters mentioned above (*85*). Fecal pellets were collected on the indicated days. Serum was collected via heart puncture postketamine/xylazine anesthesia. After cervical dislocation, the small intestine and colon length were measured, and the intestinal content was collected. For disulfiram treatment, mice were intraperitoneally injected daily with disulfiram [50 mg/kg; HY-B0240, MedChemExpress (MCE)] or vehicle (10% dimethyl sulfoxide + 90% corn oil) for the indicated period.

Whole abdomen irradiation model

Both male and female cohoused littermates were anesthetized by ketamine and xylazine, and to avoid bone marrow failure and specifically irradiate in the abdominal cavity, the rest of the mice body was protected by lead. Whole abdomen x-ray radiation of 9 or 12 Gy was used to induce different levels of intestinal injury (Precision X-Ray), and mice were monitored until the end of the experiment.

AOM/DSS-induced colitis-associated CRC model

Male cohoused littermates were intraperitoneally injected with AOM (10 mg/kg; A5486, Sigma-Aldrich) on day 0. One week after, mice were provided 3% DSS for 3 days, followed by 2 weeks of normal drinking water, which was repeated for 2 or 3 cycles as indicated. All mice were euthanized and dissected at the indicated day, the colon was collected, and the tumors were measured. Histopathology and immunofluorescence (IF) were analyzed.

Generation, treatment, and live imaging of intestinal organoid

Colonic crypts were isolated on the basis of a well-described protocol with modifications (*86*). Briefly, the colon was collected and flushed with ice-cold phosphate-buffered saline (PBS) to remove any remaining fecal contents, opened longitudinally, and cut into roughly 5-mm pieces. The tissue pieces were incubated in 10 ml of intestine dissociation buffer [10 mM EDTA, 1 mM dithiothreitol (DTT), 1× penicillin-streptomycin, and 10 mM Hepes in PBS] at 4°C for 90 min with gentle shaking. Next, the tissues were vigorously vortexed for 30 s and pipetted up and down for 10 times, passing it through the 70-μm strainer, and the supernatant was collected. The supernatant was centrifuged at 100*g* for 10 min and the pellet containing the crypts was collected. The pellet was resuspended with PBS, and the crypts were counted. A certain number of crypts were taken, centrifuged at 100*g* for 5 min, and suspended with complete IntestiCult Organoid Growth Medium (06005, STEMCELL) to 1000 crypts per 50 μl. Next, the crypts were mixed with an equal volume of Matrigel (356231, Corning) by pipetting up and down for 10 times. Fifty microliters of mixture was carefully pipetted into each well of a 24-well plate. After incubating at 37°C and 5% CO_2 for 10 min, 500 μl of complete IntestiCult Organoid Growth Medium containing 1× penicillin-streptomycin, 3 μM CHIR99021(HY-13076, MCE), and 10 μM Y-27632 (HY-10071, MCE) was added. Medium was refreshed with complete IntestiCult Organoid Growth Medium every 2 days until the end of the experiment. For organoid growth assay, the images of organoids were captured daily by Incucyte S3 (Sartorius). For cytokine and DSS treatment assay, colonic organoids were treated with murine TNF (315-01A, Thermo Fisher Scientific) and murine interferon gamma (315-05, Thermo Fisher Scientific) or 0.001% DSS on day 4.

Organoid viability quantification

Organoid death rate was quantified using Ilastik (version 1.4.0). A multistep workflow involved the following: (i) autocontext pixel classification to generate organoid boundary probability maps; (ii) multicut for boundary-based segmentation; and (iii) object classification to categorize segmented organoids as alive or dead. Trained models were used for batch processing (*87*).

High-resolution colon endoscopy

Mice were fasted for 4 hours and anesthetized with 2% isoflurane. High-resolution mouse endoscopy was performed as previously described (*88*) with the COLOVIEW endoscopic system (Karl Storz).

Intestinal permeability assay

Mice were fasted for 4 hours and gavaged with fluorescein isothiocyanate–dextran 4 (600 mg/kg; 46944-100MG-F, Sigma-Aldrich), and 4 hours later, fluorescence intensity of serum was measured (excitation 490 nm/emission 520 nm) by FLUOstar Omega (BMG LABTECH).

Tissue histology, immunohistochemistry, and IF

Intestinal tissues were fixed in 4% paraformaldehyde overnight, processed with the Shandon Citadel tissue processor (Thermo Fisher Scientific) by using standard methods and embedded in paraffin. Tissue blocks were sectioned into 5-μm-thick slices. H&E staining and Alcian Blue/periodic acid–Schiff staining were performed as previously described (*30*). Sections of the intestine were deparaffinized, rehydrated, and subjected to heat-induced epitope retrieval for antigen retrieval. Endogenous peroxidase activity was blocked by using 3% H_2O_2 in methanol, and nonspecific binding was blocked by blocking buffer (5% goat serum and 1% bovine serum albumin in PBS). For immunohistochemistry, the sections were then incubated overnight at 4°C with specific antibody targeting Ki67 [1:1000; 12202S, Cell Signaling Technology (CST)] in blocking buffer. Subsequently, horseradish peroxidase (HRP)–conjugated secondary antibodies were applied, and the positive signals were detected using a DAB kit (DAB, Vector, Burlingame, CA). Last, the sections were counterstained with hematoxylin for visualization. For IF, TUNEL staining was performed according to the manufacturer's instructions (In Situ Cell Death Detection Kit, TMR red, 12156792910, Roche). Procaspase-3 (1:200; 9662S, CST), procaspase-7 (house-made, 1:200), and goat anti-rabbit immunoglobulin G AF546 secondary antibody (1:500; A-11035, Thermo Fisher Scientific) were used. The sections were counterstained with 4′,6-diamidino-2-phenylindoleI (1 μg/ml; 62248, Thermo Fisher Scientific) to visualize the nuclei for 5 min. After additional washing steps, the sections were mounted with a mounting medium and coverslips. The IF image was acquired using Zeiss AxioScan Z1.

Transmission electron microscopy

Mouse distal colon tissue was cut into small pieces, immersed in a fixative solution of 2.5% glutaraldehyde and 3% formaldehyde in 0.1 M Na-cacodylate buffer, placed in a vacuum oven for 30 min, and left rotating for 3 hours at room temperature. This solution was later replaced with fresh fixative, and samples were left rotating overnight at 4°C. After washing, samples were postfixed in 1% OsO_4 with $K_3Fe(CN)_6$ in 0.1 M Na-cacodylate buffer (pH 7.2). After washing in double distilled H_2O, samples were subsequently dehydrated through a graded ethanol (EtOH) series, including a bulk staining with 2% uranyl acetate at the 50% EtOH step followed by embedding in Spurr's resin. To select the area of interest on the block and to have an overview of the phenotype, semithin sections were first cut at 0.5 μm and stained with toluidine blue. Ultrathin sections of a gold interference color were cut using an ultramicrotome (Leica EM UC6), followed by a poststaining in a Leica EM AC20 for 40 min in uranyl acetate at 20°C and for 10 min in lead stain at 20°C. Sections were collected on formvar-coated copper slot grids. Grids were viewed with a JEM 1400plus transmission electron microscope (JEOL, Tokyo, Japan) operating at 80 kV.

Scanning electron microscopy

The method was described in detail previously (*30*). Freshly isolated colon samples were incubated in freshly prepared fixative [2% paraformaldehyde [Electron Microscopy Sciences (EMS)] and 2.5% glutaraldehyde (EMS) in 0.1 M sodium cacodylate (EMS) buffer (pH 7.4)] overnight at 4°C. After washing 5 × 3 min in 0.1 M cacodylate buffer and incubated in 2% osmium (OsO_4, EMS) in 0.1 M cacodylate buffer for 30 min at room temperature, samples were washed in H_2O for 3 × 5 min and dehydrated using solutions of increasing EtOH concentration (50, 70, 85, 95, and 2× 100%), for 15 min each. Next, samples were dehydrated in EtOH:acetone (1:1) for 15 min, followed by 100% acetone for 15 min. The samples were then dried in a critical point dryer (Leica EM CPD300) and mounted on an aluminum stub (EMS) using carbon adhesive tape (EMS); afterward, samples were coated with 5 nm of platinum (Quorum Q150T ES). SEM 5 imaging was performed using a Zeiss Crossbeam 540.

IEC isolation

Briefly, distal colon was collected and flushed with ice-cold PBS to remove any remaining fecal contents, opened longitudinally, and cut into roughly 3-mm small pieces. The tissue pieces were incubated in 10 ml of IEC isolation buffer (5 mM EDTA, 1 μM emricasan, 10 μM Y-27632, 1 mM DTT, 10 mM Hepes, and penicillin-streptomycin in PBS) at 4°C for 90 min with gentle shaking. Next, the tissues were vigorously vortexed for 5 s and passed through a 1000-μm strainer (43-51000-50, pluriSelect), and the supernatant was collected. Tissues were transferred to a fresh tube containing 10 ml of cold PBS, vortexed for 30 s, and pipetted up and down 10 times with prewet serological pipettes, and after passing a 1000-μm strainer and collecting the supernatant, the remaining tissues were discarded. The supernatant was centrifuged at 600*g* for 10 min at 4°C and the pellet was collected. The pellet was resuspended with 10 ml of cold PBS, and passed through a 70-μm strainer. This suspension was centrifuged at 600*g* for 10 min at 4°C and IECs in the pellet were collected for further analysis.

Mouse RNA extraction and RT-qPCR

For colon tissue RNA extraction, 5-mm distal colon was placed in a 2-ml microcentrifuge tube containing one stainless steel bead (5-mm mean diameter), 150 μl of Buffer RLT per tube was added, and the TissueLyser II was operated for 5 min at 20 Hz to generate tissue homogenate. The homogenate was kept on ice for 10 min, centrifuged at 12,000*g* for 10 min at 4°C, and supernatant was collected. For IECs RNA extraction, the pellet containing IECs was directly lysed with 150 μl of Buffer RLT. Next, total RNA was isolated by using the RNeasy Micro Kit (74004, QIAGEN) according to the manufacturer's instructions. For cDNA synthesis, 200 to 1000 ng of total RNA was reverse transcribed using the Sensifast cDNA Synthesis Kit (BIO-65054, GC Biotech BV). Quantitative reverse transcription polymerase chain reaction (RT-qPCR) was performed to analyze the expression levels of specific genes. The RT-qPCR reactions were conducted using the Roche LightCycler 480 with the SensiFAST SYBR No-ROX Kit (BIO-98020, GC Biotech BV).

The relative expression levels of the target genes were determined using the comparative CT (cycle threshold) method. The expression data were normalized to the internal control *Actb* or *Hprt*. The Supplementary Materials (table S1) provide qPCR primers used in this study.

Bulk RNA-seq

One hundred nanograms of total RNA was processed by Novogene for bulk mRNA sequencing. The samples (RNA isolated from colon tissue or colon IECs of $Casp3/7^{\Delta IEC}$ mice and littermate controls) were sequenced using paired-end Illumina sequencing (150 nt). The set of IEC samples (five WT-control, five transgenic-control, five WT-DSS, and five transgenic-DSS) was processed by trimming the reads using Trimmomatic (v0.39) (*89*) with the following parameter settings: ILLUMINACLIP:"adapters.fa":3:30:10:2:True, SLIDINGWINDOW:5:20, MINLEN:36. The adapter sequences in the fasta file are AGATCGGAAGAGCGTCGTGTAGGGAAAGAGTGTAGATCTCGGTGGTCGCCGTATCATT (forward) and GATCGGAAGAGCACACGTCTGAACTCCAGTCACGGATGACTATCTCGTATGCCGTCTTCTGCTTG (reverse). Read mapping was performed using STAR (v2.7.8a) (*90*) on the GRCm39 mouse genome. Only uniquely mapped reads were kept by setting --outFilterMultimapNmax 1.

BAM files were read into an R (v4.4) environment, and a count table was made using the SummarizeOverlaps function (mode = "Union") of the GenomicAlignments (*91*) package and the GRCm39 gene annotation of Ensembl version 106. One WT DSS and one transgenic DSS (DSS_Seq1_12 and DSS_Seq1_15) samples were excluded on the basis of principal components analysis. DESeq2 (*82*) was used for differential expression analysis. Last, GSEA analysis was performed on the DE genes ($|\log_2$fold change$| > 0.5$, adjusted P value < 0.05) using fgsea (*92*) package with the Molecular Signatures Database (MSIGDB) (*93*) hallmark gene sets. The set of colon tissue samples (five day 0–WT, six day 0–transgenic, five day 8–WT, and six day 8–transgenic) was processed similarly with the following changes: The trimming step was omitted, and DESeq2 analysis was done per time point rather than on all samples at once.

Western blotting

Cells were lysed in radioimmunoprecipitation assay (RIPA) lysis buffer consisting of Protease Inhibitor Cocktail (5056489001, Sigma-Aldrich) and PhosSTOP (4906837001, Sigma-Aldrich) for 30 min on ice and centrifuged at 12,000*g* for 10 min at 4°C, and the supernatant was collected. The protein concentrations were determined by using a bicinchoninic acid assay and further diluted with RIPA buffer to achieve an equal concentration. Next, samples were mixed with Laemmli buffer, boiled at 95°C for 10 min, further loaded onto SDS–polyacrylamide gel electrophoresis gels, and transferred to a polyvinylidene difluoride membrane (Millipore). After blocking, proteins were probed by the following primary antibodies: caspase-1 (1:2000; VIB Core), caspase-3 (1:1000; 9662, CST), caspase-7 (1:1000; 9492S, CST), caspase-8 (1:1000; MAB3429, Abnova), clcaspase-8 (1:1000; 9429, CST), caspase-9 (1:1000; 9508, CST), caspase-11 (1:200; NB120-10454, NOVUS), pRIPK1 (Ser^{166}) (1:1000; 53286S, CST), RIPK1 (1:1000; 3493, CST), pRIPK3 (Thr^{231}/Ser^{232}) (1:1000; 57220, CST), pMLKL (Ser^{345}) (1:1000; 37333, CST), MLKL (1:1000; MABC604, Millipore), GSDMD (1:1000; ab209845, Abcam), GSDME (1:500; 13075-1-AP, Proteintech), GPX4 (1:5000; ab125066, Abcam), vinculin (1:200; V9131, Sigma-Aldrich), β-tubulin HRP (1:10,000; ab21058, Abcam), and β-actin HRP (1:5000; 5125, CST); followed by HRP-conjugated secondary antibody (GE Healthcare) incubation. Detection was performed with the Western Lightning chemiluminescent reagent plus kit (NEL105001EA, PerkinElmer). Immortalized mouse embryonic fibroblasts used as positive controls were created in-house. Bone marrow–derived macrophages were derived from mouse bone marrow with macrophage colony-stimulating factor.

Statistical analysis

Ki67-positive cells and TUNEL-positive cells were quantified on the basis of the selected region of interest in QuPath software, relative to the chosen area. Statistical analysis was conducted using GraphPad Prism 8.0 software. The number of replicates (*n*) in figure legends refers to biological replicates unless specified otherwise. The number of independent experiments is mentioned in the corresponding figure legends. All data are expressed as means ± SEM or SD as indicated. Group comparisons were analyzed using unpaired two-tailed Student's *t* tests if two conditions were evaluated and one-way analysis of variance (ANOVA) if three conditions were evaluated. Changes over time such as body weight were tested using two-way ANOVA or mixed-effects model (restricted maximum likelihood) analysis if data points were missing. *P* values were indicated in every comparison. With regard to statistical testing of mouse data, randomization was performed for mouse allocation. Blinding was not performed during measurements. Sample size was calculated by power analysis or on the basis of availability.

Supplementary Materials

The PDF file includes:

Figs. S1 to S6
Table S1
Legends for data files S1 and S2
Data file S3

Other Supplementary Material for this manuscript includes the following:

Data files S1 and S2

REFERENCES

1. L. G. van der Flier, H. Clevers, Stem cells, self-renewal, and differentiation in the intestinal epithelium. *Annu. Rev. Physiol.* **71**, 241–260 (2009).
2. H. Gehart, H. Clevers, Tales from the crypt: New insights into intestinal stem cells. *Nat. Rev. Gastroenterol. Hepatol.* **16**, 19–34 (2019).
3. J. Beumer, H. Clevers, Cell fate specification and differentiation in the adult mammalian intestine. *Nat. Rev. Mol. Cell Biol.* **22**, 39–53 (2021).
4. J. M. Allaire, S. M. Crowley, H. T. Law, S.-Y. Chang, H.-J. Ko, B. A. Vallance, The intestinal epithelium: Central coordinator of mucosal immunity. *Trends Immunol.* **39**, 677–696 (2018).
5. M. Schirmer, A. Garner, H. Vlamakis, R. J. Xavier, Microbial genes and pathways in inflammatory bowel disease. *Nat. Rev. Microbiol.* **17**, 497–511 (2019).
6. G. Roda, S. Chien Ng, P. G. Kotze, M. Argollo, R. Panaccione, A. Spinelli, A. Kaser, L. Peyrin-Biroulet, S. Danese, Crohn's disease. *Nat. Rev. Dis. Primers* **6**, 22 (2020).
7. T. Kobayashi, B. Siegmund, C. Le Berre, S. C. Wei, M. Ferrante, B. Shen, C. N. Bernstein, S. Danese, L. Peyrin-Biroulet, T. Hibi, Ulcerative colitis. *Nat. Rev. Dis. Primers* **6**, 74 (2020).
8. J. M. Blander, On cell death in the intestinal epithelium and its impact on gut homeostasis. *Curr. Opin. Gastroenterol.* **34**, 413–419 (2018).
9. A. Wahida, M. Müller, A. Hiergeist, B. Popper, K. Steiger, C. Branca, M. Tschurtschenthaler, T. Engleitner, S. Donakonda, J. De Coninck, R. Öllinger, M. K. Pfautsch, N. Müller, M. Silva, S. Usluer, E. Thiele Orberg, J. P. Böttcher, N. Pfarr, M. Anton, J. B. Slotta-Huspenina, A. G. Nerlich, T. Madl, M. Basic, A. Bleich, G. Berx, J. Ruland, P. A. Knolle, R. Rad, T. E. Adolph, P. Vandenabeele, H. Kanegane, A. Gessner, P. J. Jost, M. Yabal, XIAP restrains TNF-driven intestinal inflammation and dysbiosis by promoting innate immune responses of Paneth and dendritic cells. *Sci. Immunol.* **6**, eabf7235 (2021).
10. J. V. Patankar, C. Becker, Cell death in the gut epithelium and implications for chronic inflammation. *Nat. Rev. Gastroenterol. Hepatol.* **17**, 543–556 (2020).
11. R. Wang, H. Li, J. Wu, Z.-Y. Cai, B. Li, H. Ni, X. Qiu, H. Chen, W. Liu, Z.-H. Yang, M. Liu, J. Hu, Y. Liang, P. Lan, J. Han, W. Mo, Gut stem cell necroptosis by genome instability triggers bowel inflammation. *Nature* **580**, 386–390 (2020).
12. G. Tan, C. Huang, J. Chen, F. Zhi, HMGB1 released from GSDME-mediated pyroptotic epithelial cells participates in the tumorigenesis of colitis-associated colorectal cancer through the ERK1/2 pathway. *J. Hematol. Oncol.* **13**, 149 (2020).
13. M. Xu, J. Tao, Y. Yang, S. Tan, H. Liu, J. Jiang, F. Zheng, B. Wu, Ferroptosis involves in intestinal epithelial cell death in ulcerative colitis. *Cell Death Dis.* **11**, 86 (2020).
14. J. Pang, A. H. Al-Ani, K. M. Patel, S. N. Young, I. Kong, J.-J. Chen, M. Barrios, J. A. Rickard, S. Chen, S. Foroughi, W. Cawthorne, A. V. Jacobsen, A. Jois, A. L. Weir, L. W. Whitehead, P. Rajasekhar, C. R. Horne, I. Azeez, T. Tan, W. Liang, S. Sivanesan, A. Metz, A. Patwardhan, N. Shea, G. Iyngkaran, D. Schneider, A. T. Elford, W. Beattie, F. Macrae, G. Liccardi, H. Walczak, Y. Zhang, O. M. Sieber, T. Spelman, L. Giulino-Roth, E. D. Hawkins, K. L. Rogers, R. Bowden, S. E. Nicholson, K. E. Lawlor, B. Christensen, A. L. Samson, J. E. Vince, J. M. Murphy, A necroptotic-to-apoptotic signaling axis underlies inflammatory bowel disease. bioRxiv 623307 [Preprint] (2024). https://doi.org/10.1101/2024.11.13.623307.
15. K. Nozaki, V. I. Maltez, M. Rayamajhi, A. L. Tubbs, J. E. Mitchell, C. A. Lacey, C. K. Harvest, L. Li, W. T. Nash, H. N. Larson, B. D. McGlaughon, N. J. Moorman, M. G. Brown, J. K. Whitmire, E. A. Miao, Caspase-7 activates ASM to repair gasdermin and perforin pores. *Nature* **606**, 960–967 (2022).
16. S. H. Lee, J. Y. Kwon, J. Moon, J. Choi, J. Jhun, K. Jung, K.-H. Cho, O. Darlami, H. H. Lee, E. S. Jung, D. Y. Shin, B.-I. Lee, M.-L. Cho, Inhibition of RIPK3 pathway attenuates intestinal inflammation and cell death of inflammatory bowel disease and suppresses necroptosis in peripheral mononuclear cells of ulcerative colitis patients. *Immune Netw.* **20**, e16 (2020).
17. J. Söderman, L. Berglind, S. Almer, Gene expression-genotype analysis implicates GSDMA, GSDMB, and LRRC3C as contributors to inflammatory bowel disease susceptibility. *Biomed. Res. Int.* **2015**, 834805 (2015).
18. K. Bulek, J. Zhao, Y. Liao, N. Rana, D. Corridoni, A. Antanaviciute, X. Chen, H. Wang, W. Qian, W. A. Miller-Little, S. Swaidani, F. Tang, B. B. Willard, K. McCrae, Z. Kang, G. R. Dubyak, F. Cominelli, A. Simmons, T. T. Pizarro, X. Li, Epithelial-derived gasdermin D mediates nonlytic IL-1β release during experimental colitis. *J. Clin. Invest.* **130**, 4218–4234 (2020).
19. G. Tan, C. Huang, J. Chen, B. Chen, F. Zhi, Gasdermin-E-mediated pyroptosis participates in the pathogenesis of Crohn's disease by promoting intestinal inflammation. *Cell Rep.* **35**, 109265 (2021).
20. L. Mayr, F. Grabherr, J. Schwärzler, I. Reitmeier, F. Sommer, T. Gehmacher, L. Niederreiter, G.-W. He, B. Ruder, K. T. R. Kunz, P. Tymoszuk, R. Hilbe, D. Haschka, C. Feistritzer, R. R. Gerner, B. Enrich, N. Przysiecki, M. Seifert, M. A. Keller, G. Oberhuber, S. Sprung, Q. Ran, R. Koch, M. Effenberger, I. Tancevski, H. Zoller, A. R. Moschen, G. Weiss, C. Becker, P. Rosenstiel, A. Kaser, H. Tilg, T. E. Adolph, Dietary lipids fuel GPX4-restricted enteritis resembling Crohn's disease. *Nat. Commun.* **11**, 1775 (2020).
21. J. Yuan, D. Ofengeim, A guide to cell death pathways. *Nat. Rev. Mol. Cell Biol.* **25**, 379–395 (2024).
22. O. Julien, M. Zhuang, A. P. Wiita, A. J. O'Donoghue, G. M. Knudsen, C. S. Craik, J. A. Wells, Quantitative MS-based enzymology of caspases reveals distinct protein substrate specificities, hierarchies, and cellular roles. *Proc. Natl. Acad. Sci. U.S.A.* **113**, E2001–E2010 (2016).
23. S. M. Man, T.-D. Kanneganti, Converging roles of caspases in inflammasome activation, cell death and innate immunity. *Nat. Rev. Immunol.* **16**, 7–21 (2016).
24. M. Sarji, R. Ankawa, M. Yampolsky, Y. Fuchs, A near death experience: The secret stem cell life of caspase-3. *Semin. Cell Dev. Biol.* **171**, 103617 (2025).
25. Y. Yosefzon, D. Soteriou, A. Feldman, L. Kostic, E. Koren, S. Brown, R. Ankawa, E. Sedov, F. Glaser, Y. Fuchs, Caspase-3 regulates YAP-dependent cell proliferation and organ size. *Mol. Cell* **70**, 573–587.e4 (2018).
26. Y. Yosefzon, Y. Fuchs, Exiting the dark side: A vital role for caspase-3 in Yap signaling. *Mol. Cell. Oncol.* **5**, e1494947 (2018).
27. C. Zhu, F. Fan, C.-Y. Li, Y. Xiong, X. Liu, Caspase-3 promotes oncogene-induced malignant transformation via EndoG-dependent Src-STAT3 phosphorylation. *Cell Death Dis.* **15**, 486 (2024).
28. J. R. García-Lozano, B. Torres, O. Fernández, G. Orozco, A. Alvarez-Márquez, A. García, M. A. González-Gay, A. García, A. Núñez-Roldán, J. Martín, M. F. González-Escribano, Caspase 7 influences susceptibility to rheumatoid arthritis. *Rheumatology* **46**, 1243–1247 (2007).
29. A. Akhter, M. A. Gavrilin, L. Frantz, S. Washington, C. Ditty, D. Limoli, C. Day, A. Sarkar, C. Newland, J. Butchar, C. B. Marsh, M. D. Wewers, S. Tridandapani, T.-D. Kanneganti, A. O. Amer, Caspase-7 activation by the Nlrc4/Ipaf inflammasome restricts *Legionella pneumophila* infection. *PLOS Pathog.* **5**, e1000361 (2009).
30. F. Ghazavi, J. Huysentruyt, J. De Coninck, S. Kourula, S. Martens, B. Hassannia, T. Wartewig, T. Divert, R. Roelandt, B. Popper, A. Hiergeist, P. Tougaard, T. Vanden Berghe, M. Joossens, G. Berx, N. Takahashi, A. Wahida, P. Vandenabeele, Executioner caspases 3 and 7 are dispensable for intestinal epithelium turnover and homeostasis at steady state. *Proc. Natl. Acad. Sci. U.S.A.* **119**, e2024508119 (2022).
31. C. J. Anderson, L. Boeckaerts, P. Chin, J. B. Cardas, W. Xie, A. Gonçalves, G. Blancke, S. Benson, S. Rogatti, M. S. Simpson, A. Davey, S. M. Choi, S. Desmet, S. D. Bushman, G. Goeminne, P. Vandenabeele, M. S. Desai, L. Vereecke, K. S. Ravichandran, Metabolite-based inter-kingdom communication controls intestinal tissue recovery following chemotherapeutic injury. *Cell Host Microbe* **32**, 1469–1487.e9 (2024).
32. P. H. V. Saavedra, L. Huang, F. Ghazavi, S. Kourula, T. Vanden Berghe, N. Takahashi, P. Vandenabeele, M. Lamkanfi, Apoptosis of intestinal epithelial cells restricts Clostridium difficile infection in a model of pseudomembranous colitis. *Nat. Commun.* **9**, 4846 (2018).
33. H. Khalil, N. Peltzer, J. Walicki, J.-Y. Yang, G. Dubuis, N. Gardiol, W. Held, P. Bigliardi, B. Marsland, L. Liaudet, C. Widmann, Caspase-3 protects stressed organs against cell death. *Mol. Cell. Biol.* **32**, 4523–4533 (2012).
34. D. Hong, H. K. Kim, W. Yang, C. Yoon, M. Kim, C.-S. Yang, S. Yoon, Integrative analysis of single-cell RNA-seq and gut microbiome metabarcoding data elucidates macrophage dysfunction in mice with DSS-induced ulcerative colitis. *Commun. Biol.* **7**, 731 (2024).
35. Y.-T. Ho, T. Shimbo, E. Wijaya, T. Kitayama, S. Takaki, K. Ikegami, K. Miyashita, Y. Ouchi, E. Takaki, R. Yamamoto, Y. Kaneda, K. Tamai, Longitudinal single-cell transcriptomics reveals a role for Serpina3n-mediated resolution of inflammation in a mouse colitis model. *Cell. Mol. Gastroenterol. Hepatol.* **12**, 547–566 (2021).

36. L. Schulte, M. Hohwieler, M. Müller, J. Klaus, Intestinal organoids as a novel complementary model to dissect inflammatory bowel disease. *Stem Cells Int.* **2019**, 8010645 (2019).
37. H. R. Rallabandi, H. Yang, K. B. Oh, H. C. Lee, S. J. Byun, B. R. Lee, Evaluation of intestinal epithelial barrier function in inflammatory bowel diseases using Murine intestinal organoids. *Tissue Eng. Regen. Med.* **17**, 641–650 (2020).
38. R. Dirisina, R. B. Katzman, T. Goretsky, E. Managlia, N. Mittal, D. B. Williams, W. Qiu, J. Yu, N. S. Chandel, L. Zhang, T. A. Barrett, p53 and PUMA independently regulate apoptosis of intestinal epithelial cells in patients and mice with colitis. *Gastroenterology* **141**, 1036–1045 (2011).
39. N. Kayagaki, I. B. Stowe, B. L. Lee, K. O'Rourke, K. Anderson, S. Warming, T. Cuellar, B. Haley, M. Roose-Girma, Q. T. Phung, P. S. Liu, J. R. Lill, H. Li, J. Wu, S. Kummerfeld, J. Zhang, W. P. Lee, S. J. Snipas, G. S. Salvesen, L. X. Morris, L. Fitzgerald, Y. Zhang, E. M. Bertram, C. C. Goodnow, V. M. Dixit, Caspase-11 cleaves gasdermin D for non-canonical inflammasome signalling. *Nature* **526**, 666–671 (2015).
40. J. Shi, Y. Zhao, K. Wang, X. Shi, Y. Wang, H. Huang, Y. Zhuang, T. Cai, F. Wang, F. Shao, Cleavage of GSDMD by inflammatory caspases determines pyroptotic cell death. *Nature* **526**, 660–665 (2015).
41. Z. Liu, C. Wang, J. Yang, Y. Chen, B. Zhou, D. W. Abbott, T. S. Xiao, Caspase-1 engages full-length gasdermin D through two distinct interfaces that mediate caspase recruitment and substrate cleavage. *Immunity* **53**, 106–114.e5 (2020).
42. C. Y. Taabazuing, M. C. Okondo, D. A. Bachovchin, Pyroptosis and apoptosis pathways engage in bidirectional crosstalk in monocytes and macrophages. *Cell Chem. Biol.* **24**, 507–514.e4 (2017).
43. S. S. Wright, C. Wang, A. Ta, M. S. Havira, J. Ruan, V. A. Rathinam, S. K. Vanaja, A bacterial toxin co-opts caspase-3 to disable active gasdermin D and limit macrophage pyroptosis. *Cell Rep.* **43**, 114004 (2024).
44. J. J. Hu, X. Liu, S. Xia, Z. Zhang, Y. Zhang, J. Zhao, J. Ruan, X. Luo, X. Lou, Y. Bai, J. Wang, L. R. Hollingsworth, V. G. Magupalli, L. Zhao, H. R. Luo, J. Kim, J. Lieberman, H. Wu, FDA-approved disulfiram inhibits pyroptosis by blocking gasdermin D pore formation. *Nat. Immunol.* **21**, 736–745 (2020).
45. J. K. Rathkey, J. Zhao, Z. Liu, Y. Chen, J. Yang, H. C. Kondolf, B. L. Benson, S. M. Chirieleison, A. Y. Huang, G. R. Dubyak, T. S. Xiao, X. Li, D. W. Abbott, Chemical disruption of the pyroptotic pore-forming protein gasdermin D inhibits inflammatory cell death and sepsis. *Sci. Immunol.* **3**, eaat2738 (2018).
46. C. Juliana, T. Fernandes-Alnemri, J. Wu, P. Datta, L. Solorzano, J.-W. Yu, R. Meng, A. A. Quong, E. Latz, C. P. Scott, E. S. Alnemri, Anti-inflammatory compounds parthenolide and Bay 11-7082 are direct inhibitors of the inflammasome. *J. Biol. Chem.* **285**, 9792–9802 (2010).
47. M. W. M. D. Lutgens, F. P. Vleggaar, M. E. I. Schipper, P. C. F. Stokkers, C. J. van der Woude, D. W. Hommes, D. J. de Jong, G. Dijkstra, A. A. van Bodegraven, B. Oldenburg, M. Samsom, High frequency of early colorectal cancer in inflammatory bowel disease. *Gut* **57**, 1246–1251 (2008).
48. T. Jess, C. Rungoe, L. Peyrin-Biroulet, Risk of colorectal cancer in patients with ulcerative colitis: A meta-analysis of population-based cohort studies. *Clin. Gastroenterol. Hepatol.* **10**, 639–645 (2012).
49. L. F. Ye, K. R. Chaudhary, F. Zandkarimi, A. D. Harken, C. J. Kinslow, P. S. Upadhyayula, A. Dovas, D. M. Higgins, H. Tan, Y. Zhang, M. Buonanno, T. J. C. Wang, T. K. Hei, J. N. Bruce, P. D. Canoll, S. K. Cheng, B. R. Stockwell, Radiation-induced lipid peroxidation triggers ferroptosis and synergizes with ferroptosis inducers. *ACS Chem. Biol.* **15**, 469–484 (2020).
50. G. Lei, Y. Zhang, P. Koppula, X. Liu, J. Zhang, S. H. Lin, J. A. Ajani, Q. Xiao, Z. Liao, H. Wang, B. Gan, The role of ferroptosis in ionizing radiation-induced cell death and tumor suppression. *Cell Res.* **30**, 146–162 (2020).
51. Q. Zhou, Y. Meng, D. Li, L. Yao, J. Le, Y. Liu, Y. Sun, F. Zeng, X. Chen, G. Deng, Ferroptosis in cancer: From molecular mechanisms to therapeutic strategies. *Signal Transduct. Target. Ther.* **9**, 55 (2024).
52. C. E. Berry, C. B. Kendig, N. An, A. Z. Fazilat, A. A. Churukian, M. Griffin, P. M. Pan, M. T. Longaker, S. J. Dixon, D. C. Wan, Role of ferroptosis in radiation-induced soft tissue injury. *Cell Death Discov.* **10**, 313 (2024).
53. L. Wang, A. Wang, Q. Fu, Z. Shi, X. Chen, Y. Wang, W. Xu, T. Wang, S. Zhang, S. Hu, Ferroptosis plays an important role in promoting ionizing radiation-induced intestinal injuries. *Biochem. Biophys. Res. Commun.* **595**, 7–13 (2022).
54. Q. Ji, S. Fu, H. Zuo, Y. Huang, L. Chu, Y. Zhu, J. Hu, Y. Wu, S. Chen, Y. Wang, Y. Ren, X. Pu, N. Liu, R. Li, X. Wang, C. Dai, ACSL4 is essential for radiation-induced intestinal injury by initiating ferroptosis. *Cell Death Discov.* **8**, 332 (2022).
55. H. Zhou, Y.-L. Zhou, J.-A. Mao, L.-F. Tang, J. Xu, Z.-X. Wang, Y. He, M. Li, NCOA4-mediated ferritinophagy is involved in ionizing radiation-induced ferroptosis of intestinal epithelial cells. *Redox Biol.* **55**, 102413 (2022).
56. F. Zhang, T. Liu, H.-C. Huang, Y.-Y. Zhao, M. He, W. Yuan, L. Li, J. Li, D.-M. Wu, Y. Xu, Activation of pyroptosis and ferroptosis is involved in radiation-induced intestinal injury in mice. *Biochem. Biophys. Res. Commun.* **631**, 102–109 (2022).
57. J. Yang, J. Mo, J. Dai, C. Ye, W. Cen, X. Zheng, L. Jiang, L. Ye, Cetuximab promotes RSL3-induced ferroptosis by suppressing the Nrf2/HO-1 signalling pathway in KRAS mutant colorectal cancer. *Cell Death Dis.* **12**, 1079 (2021).
58. S. L. DeAngelo, L. Zhao, S. Dziechciarz, M. Shin, S. Solanki, A. Balia, M. O. El-Derany, C. Castillo, Y. Qin, N. K. Das, H. N. Bell, J. A. Paulo, Y. Zhang, N. J. Rossiter, E. C. McCulla, J. He, I. Talukder, B. W.-L. Ng, Z. T. Schafer, N. Neamati, J. D. Mancias, M. Koutmos, Y. M. Shah, Recharacterization of the tumor suppressive mechanism of RSL3 identifies the selenoproteome as a druggable pathway in colorectal cancer. *Cancer Res.* **85**, 2788–2804 (2025).
59. T. Kawaue, I. Yow, Y. Pan, A. P. Le, Y. Lou, M. Loberas, M. Shagirov, X. Teng, J. Prost, T. Hiraiwa, B. Ladoux, Y. Toyama, Inhomogeneous mechanotransduction defines the spatial pattern of apoptosis-induced compensatory proliferation. *Dev. Cell* **58**, 267–277.e5 (2023).
60. K. Rajagopalan, J. D. Selvan Christyraj, K. S. Chelladurai, K. Kalimuthu, P. Das, M. Chandrasekar, N. Balamurugan, K. Murugan, Understanding the molecular mechanism of regeneration through apoptosis-induced compensatory proliferation studies - updates and future aspects. *Apoptosis* **29**, 1399–1414 (2024).
61. E. Eskandari, C. J. Eaves, Paradoxical roles of caspase-3 in regulating cell survival, proliferation, and tumorigenesis. *J. Cell Biol.* **221**, e202201159 (2022).
62. X. Liu, Y. He, F. Li, Q. Huang, T. A. Kato, R. P. Hall, C.-Y. Li, Caspase-3 promotes genetic instability and carcinogenesis. *Mol. Cell* **58**, 284–296 (2015).
63. Q. Pan, X. Lou, J. Zhang, Y. Zhu, F. Li, Q. Shan, X. Chen, Y. Xie, S. Su, H. Wei, L. Lin, L. Wu, S. Liu, Genomic variants in mouse model induced by azoxymethane and dextran sodium sulfate improperly mimic human colorectal cancer. *Sci. Rep.* **7**, 25 (2017).
64. L. J. Yant, Q. Ran, L. Rao, H. Van Remmen, T. Shibatani, J. G. Belter, L. Motta, A. Richardson, T. A. Prolla, The selenoprotein GPX4 is essential for mouse development and protects from radiation and oxidative damage insults. *Free Radic. Biol. Med.* **34**, 496–502 (2003).
65. H. Imai, F. Hirao, T. Sakamoto, K. Sekine, Y. Mizukura, M. Saito, T. Kitamoto, M. Hayasaka, K. Hanaoka, Y. Nakagawa, Early embryonic lethality caused by targeted disruption of the mouse PHGPx gene. *Biochem. Biophys. Res. Commun.* **305**, 278–286 (2003).
66. A. Seiler, M. Schneider, H. Förster, S. Roth, E. K. Wirth, C. Culmsee, N. Plesnila, E. Kremmer, O. Rådmark, W. Wurst, G. W. Bornkamm, U. Schweizer, M. Conrad, Glutathione peroxidase 4 senses and translates oxidative stress into 12/15-lipoxygenase dependent- and AIF-mediated cell death. *Cell Metab.* **8**, 237–248 (2008).
67. J. P. Friedmann Angeli, M. Schneider, B. Proneth, Y. Y. Tyurina, V. A. Tyurin, V. J. Hammond, N. Herbach, M. Aichler, A. Walch, E. Eggenhofer, D. Basavarajappa, O. Rådmark, S. Kobayashi, T. Seibt, H. Beck, F. Neff, I. Esposito, R. Wanke, H. Förster, O. Yefremova, M. Heinrichmeyer, G. W. Bornkamm, E. K. Geissler, S. B. Thomas, B. R. Stockwell, V. B. O'Donnell, V. E. Kagan, J. A. Schick, M. Conrad, Inactivation of the ferroptosis regulator Gpx4 triggers acute renal failure in mice. *Nat. Cell Biol.* **16**, 1180–1191 (2014).
68. W. S. Yang, R. SriRamaratnam, M. E. Welsch, K. Shimada, R. Skouta, V. S. Viswanathan, J. H. Cheah, P. A. Clemons, A. F. Shamji, C. B. Clish, L. M. Brown, A. W. Girotti, V. W. Cornish, S. L. Schreiber, B. R. Stockwell, Regulation of ferroptotic cancer cell death by GPX4. *Cell* **156**, 317–331 (2014).
69. V. E. Kagan, G. Mao, F. Qu, J. P. F. Angeli, S. Doll, C. S. Croix, H. H. Dar, B. Liu, V. A. Tyurin, V. B. Ritov, A. A. Kapralov, A. A. Amoscato, J. Jiang, T. Anthonymuthu, D. Mohammadyani, Q. Yang, B. Proneth, J. Klein-Seetharaman, S. Watkins, I. Bahar, J. Greenberger, R. K. Mallampalli, B. R. Stockwell, Y. Y. Tyurina, M. Conrad, H. Bayır, Oxidized arachidonic and adrenic PEs navigate cells to ferroptosis. *Nat. Chem. Biol.* **13**, 81–90 (2017).
70. S. J. Dixon, J. A. Olzmann, The cell biology of ferroptosis. *Nat. Rev. Mol. Cell Biol.* **25**, 424–442 (2024).
71. X. Wang, W. Li, Y. Dong, Y. Zhang, Q. Huo, L. Lu, J. Zhang, Y. Zhao, S. Fan, H. Dong, D. Li, Ferrostatin-1 mitigates ionizing radiation-induced intestinal injuries by inhibiting apoptosis and ferroptosis: An in vitro and in vivo study. *Int. J. Radiat. Biol.* **99**, 1607–1618 (2023).
72. C. Huang, L. Zhang, P. Shen, Z. Wu, G. Li, Y. Huang, T. Ao, L. Luo, C. Hu, N. Wang, R. Quzhuo, L. Tian, C. Huangfu, Z. Liao, Y. Gao, Cannabidiol mitigates radiation-induced intestine ferroptosis via facilitating the heterodimerization of RUNX3 with CBFβ thereby promoting transactivation of GPX4. *Free Radic. Biol. Med.* **222**, 288–303 (2024).
73. T. Nakamura, M. Conrad, Exploiting ferroptosis vulnerabilities in cancer. *Nat. Cell Biol.* **26**, 1407–1419 (2024).
74. A. Wahida, M. Conrad, Decoding ferroptosis for cancer therapy. *Nat. Rev. Cancer* **25**, 910–924 (2025).
75. J. M. Ubellacker, S. J. Dixon, Prospects for ferroptosis therapies in cancer. *Nat. Cancer* **6**, 1326–1336 (2025).
76. X. Zhang, Y. Ma, J. Ma, L. Yang, Q. Song, H. Wang, G. Lv, Glutathione peroxidase 4 as a therapeutic target for anti-colorectal cancer drug-tolerant persister cells. *Front. Oncol.* **12**, 913669 (2022).
77. W. Zhao, Q. Yan, L. Liu, D. Hou, D. Xiang, D. Tang, L. Li, W. Shen, W. Tao, H. Cheng, D. Sun, Curcumol promotes ferroptosis of colon cancer by targeting the ubiquitination and degradation of GPX4. *J. Tradit. Complement. Med.* **15**, 170–181 (2025).

78. Z. Liu, R. Liu, H. Gao, S. Jung, X. Gao, R. Sun, X. Liu, Y. Kim, H.-S. Lee, Y. Kawai, M. Nagasaki, J. Umeno, K. Tokunaga, Y. Kinouchi, A. Masamune, W. Shi, C. Shen, Z. Guo, K. Yuan, FinnGen, International Inflammatory Bowel Disease Genetics Consortium, Chinese Inflammatory Bowel Disease Genetics Consortium, S. Zhu, D. Li, J. Liu, T. Ge, J. Cho, M. J. Daly, D. P. B. McGovern, B. D. Ye, K. Song, Y. Kakuta, M. Li, H. Huang, Genetic architecture of the inflammatory bowel diseases across East Asian and European ancestries. *Nat. Genet.* **55**, 796–806 (2023).
79. Y. Haberman, R. Karns, P. J. Dexheimer, M. Schirmer, J. Somekh, I. Jurickova, T. Braun, E. Novak, L. Bauman, M. H. Collins, A. Mo, M. J. Rosen, E. Bonkowski, N. Gotman, A. Marquis, M. Nistel, P. A. Rufo, S. S. Baker, C. G. Sauer, J. Markowitz, M. D. Pfefferkorn, J. R. Rosh, B. M. Boyle, D. R. Mack, R. N. Baldassano, S. Shah, N. S. Leleiko, M. B. Heyman, A. M. Grifiths, A. S. Patel, J. D. Noe, B. J. Aronow, S. Kugathasan, T. D. Walters, G. Gibson, S. D. Thomas, K. Mollen, S. Shen-Orr, C. Huttenhower, R. J. Xavier, J. S. Hyams, L. A. Denson, Ulcerative colitis mucosal transcriptomes reveal mitochondriopathy and personalized mechanisms underlying disease severity and treatment response. *Nat. Commun.* **10**, 38 (2019).
80. R. Pelia, S. Venkateswaran, J. D. Matthews, Y. Haberman, D. J. Cutler, J. S. Hyams, L. A. Denson, S. Kugathasan, Profiling non-coding RNA levels with clinical classifiers in pediatric Crohn's disease. *BMC Med. Genomics* **14**, 194 (2021).
81. N. Loberman-Nachum, K. Sosnovski, A. Di Segni, G. Efroni, T. Braun, M. BenShoshan, L. Anafi, C. Avivi, I. Barshack, D. S. Shouval, L. A. Denson, A. Amir, R. Unger, B. Weiss, Y. Haberman, Defining the celiac disease transcriptome using clinical pathology specimens reveals biologic pathways and supports diagnosis. *Sci. Rep.* **9**, 16163 (2019).
82. M. I. Love, W. Huber, S. Anders, Moderated estimation of fold change and dispersion for RNA-seq data with DESeq2. *Genome Biol.* **15**, 550 (2014).
83. R. Satija, J. A. Farrell, D. Gennert, A. F. Schier, A. Regev, Spatial reconstruction of single-cell gene expression data. *Nat. Biotechnol.* **33**, 495–502 (2015).
84. J. M. Murphy, P. E. Czabotar, J. M. Hildebrand, I. S. Lucet, J.-G. Zhang, S. Alvarez-Diaz, R. Lewis, N. Lalaoui, D. Metcalf, A. I. Webb, S. N. Young, L. N. Varghese, G. M. Tannahill, E. C. Hatchell, I. J. Majewski, T. Okamoto, R. C. J. Dobson, D. J. Hilton, J. J. Babon, N. A. Nicola, A. Strasser, J. Silke, W. S. Alexander, The pseudokinase MLKL mediates necroptosis via a molecular switch mechanism. *Immunity* **39**, 443–453 (2013).
85. Y. H. Park, N. Kim, Y. K. Shim, Y. J. Choi, R. H. Nam, Y. J. Choi, M. H. Ham, J. H. Suh, S. M. Lee, C. M. Lee, H. Yoon, H. S. Lee, D. H. Lee, Adequate dextran sodium sulfate-induced colitis model in mice and effective outcome measurement method. *J. Cancer Prev.* **20**, 260–267 (2015).
86. A. L. Haber, M. Biton, N. Rogel, R. H. Herbst, K. Shekhar, C. Smillie, G. Burgin, T. M. Delorey, M. R. Howitt, Y. Katz, I. Tirosh, S. Beyaz, D. Dionne, M. Zhang, R. Raychowdhury, W. S. Garrett, O. Rozenblatt-Rosen, H. N. Shi, O. Yilmaz, R. J. Xavier, A. Regev, A single-cell survey of the small intestinal epithelium. *Nature* **551**, 333–339 (2017).
87. S. Berg, D. Kutra, T. Kroeger, C. N. Straehle, B. X. Kausler, C. Haubold, M. Schiegg, J. Ales, T. Beier, M. Rudy, K. Eren, J. I. Cervantes, B. Xu, F. Beuttenmueller, A. Wolny, C. Zhang, U. Koethe, F. A. Hamprecht, A. Kreshuk, Ilastik: Interactive machine learning for (bio) image analysis. *Nat. Methods* **16**, 1226–1232 (2019).
88. C. Becker, M. C. Fantini, M. F. Neurath, High resolution colonoscopy in live mice. *Nat. Protoc.* **1**, 2900–2904 (2006).
89. A. M. Bolger, M. Lohse, B. Usadel, Trimmomatic: A flexible trimmer for Illumina sequence data. *Bioinformatics* **30**, 2114–2120 (2014).
90. A. Dobin, C. A. Davis, F. Schlesinger, J. Drenkow, C. Zaleski, S. Jha, P. Batut, M. Chaisson, T. R. Gingeras, STAR: Ultrafast universal RNA-seq aligner. *Bioinformatics* **29**, 15–21 (2013).
91. M. Lawrence, W. Huber, H. Pagès, P. Aboyoun, M. Carlson, R. Gentleman, M. T. Morgan, V. J. Carey, Software for computing and annotating genomic ranges. *PLoS Comput. Biol.* **9**, e1003118 (2013).
92. G. Korotkevich, V. Sukhov, N. Budin, B. Shpak, M. N. Artyomov, A. Sergushichev, Fast gene set enrichment analysis, bioRxiv 060012 [Preprint] (2016). https://doi.org/10.1101/060012.
93. A. Liberzon, C. Birger, H. Thorvaldsdóttir, M. Ghandi, J. P. Mesirov, P. Tamayo, The Molecular Signatures Database (MSigDB) hallmark gene set collection. *Cell Syst.* **1**, 417–425 (2015).

Acknowledgments: We thank P. Borghgraef and A. Gonçalves from VIB BioImaging Core for SEM work and image data acquisition/analysis, respectively. We thank C. J. Anderson from The University of Edinburgh for the constructive discussion and advice, L. Vereecke and V. Andries from Ghent University for support and access to the Germ-Free and Gnotobiotic Mouse Facility Ghent (GFMF), and the VIB-UGent animal house staff for support in all mouse-related work. We thank J. Murphy from WEHI and V. Dixit from Genentech for the gift of the *Mlkl*$^{-/-}$ and *Gsdme*$^{-/-}$ mice, respectively. **Funding:** This work was supported by the Research Foundation–Flanders 11H9523N (J.H.); Research Foundation–Flanders 3G033120, 3G0A9322, and 3G0AA824 (P.V.); The Excellence of Science research consortium 3G0I5722 (P.V. and M.L.); UGent Special Research Fund Methusalem 01M00709 (P.V.); Interuniversity BOF projects 01IB3920 (P.V.); Foundation against Cancer 365A08921 and 365G09122 (P.V.); Ghent University BOF23/GOA/001 (M.L.); and Research Foundation–Flanders G014221N (M.L.). **Author contributions:** W.X.: Writing—original draft, conceptualization, investigation, writing—review and editing, methodology, resources, funding acquisition, validation, formal analysis, project administration, and visualization. L.W.: Investigation. M.V.: Investigation. B.V.: Software, formal analysis, data curation, writing—review and editing, and visualization. T.D.: Investigation, resources, and validation. J.H.: Methodology and formal analysis. R.D.R.: Investigation and visualization. F.B: Visualization and resources. M.L.: Resources, writing—review and editing, and funding acquisition. G.B.: Investigation, writing—review and editing, validation, supervision, formal analysis, and project administration. A.W.: Writing—original draft, conceptualization, writing—review and editing, supervision, and visualization. P.V.: Writing—original draft, conceptualization, investigation, writing—review and editing, methodology, resources, funding acquisition, data curation, validation, supervision, and project administration. **Competing interests:** M.L. serves on the scientific advisory board of Ventyx Biosciences. All other authors declare that they have no competing interests. **Data, code, and materials availability:** All data and code needed to evaluate and reproduce the results in the paper are present in the paper and/or the Supplementary Materials. RNA-seq data were deposited in the GEO repository under accession ID GSE297859. Computer code used to analyze the sequencing data is deposited in a GitHub repository that is publicly accessible at https://github.com/UPVA-Bioinformatician/Caspase3-7-paper-scripts-. An archive of the scripts can be downloaded from Zenodo: https://doi.org/10.5281/zenodo.17466087. Mouse lines and antibodies generated for this study are available upon request by contacting the corresponding author.

Submitted 10 June 2025
Accepted 18 February 2026
Published 20 March 2026
10.1126/sciadv.adz5906

Science Advances

Caspase-3/7 deficiency results in enhanced intestinal inflammation and reduced tumorigenesis

Wei Xie, Laura Wyckaert, Mike Vadi, Bruno Verstraeten, Tatyana Divert, Jef Haerinck, Riet De Rycke, Femke Baeke, Mohamed Lamkanfi, Geert Berx, Adam Wahida, and Peter Vandenabeele

Sci. Adv. **12** (12), eadz5906. DOI: 10.1126/sciadv.adz5906

Science Advances (ISSN 2375-2548) is published by the American Association for the Advancement of Science. 1200 New York Avenue NW, Washington, DC 20005. The title *Science Advances* is a registered trademark of AAAS.